

Aeroelastic modes and flow-induced vibrations of flexible membrane wings

G. Li¹†, B. C. Khoo¹ and R. K. Jaiman²‡

¹Department of Mechanical Engineering, National University of Singapore, Singapore 119077

²Department of Mechanical Engineering, University of British Columbia, Vancouver, BC Canada V6T 1Z4

(Received xx; revised xx; accepted xx)

In this work, we numerically investigate the flow-induced vibrations (FIVs) of flexible membranes at moderate Reynolds numbers. A high-fidelity three-dimensional (3D) variational fluid-structure interaction solver based on the recently developed partitioned body-fitted formulation is employed to simulate the fluid-membrane interaction (FMI). Given the complexity of the FMI phenomenon caused by the overlap of the self-excited multiple membrane modes, we adopt a global Fourier mode decomposition (FMD) approach to identify and extract the frequency-ranked dominant aeroelastic modes. Of particular interest is to build a direct connection between the membrane vibration and the unsteady surrounding flow features to reveal the underlying aeroelastic mode selection mechanism. We find that the membrane modes are excited by the surface pressure fluctuation mode with a similar modal shape at the same energetic frequency. At a moderate angle of attack, we further investigate the evolution of the flow-induced membrane instability of a 3D flexible membrane as a function of the non-dimensional mass ratio m^* , Reynolds number Re and aeroelastic number Ae , and identify two distinctive stability regimes, namely (a) deformed-steady state (DSS) and (b) dynamic balance state (DBS). The flexible membrane leaves the static equilibrium position to vibrate in a particular vibrational mode and establishes limit-cycle oscillation (LCO) by interplaying with the local shear layer and global vortex shedding instabilities. Within the DBS regime, three distinctive unsteady vibrational modes are classified from the full-body profile responses over a wide range of m^* : (i) asymmetric chord-wise second mode, (ii) transitional mode and (iii) symmetric chord-wise first mode. With the aid of the FMD method, we explore the mode transition map at various mass ratios. The aeroelastic mode transition is quantitatively confirmed by comparing the individual mode energy distribution to the overall membrane dynamics. This mode transition phenomenon, predominately influenced by the inertial effect, is triggered by the mode synchronization between aeroelastic modes of different orders. We find that the evolution of the inherent tension and the aerodynamic load plays an important role in the aeroelastic instability. Mode transition is also observed for a heavier membrane with $m^* = 9.6$ as Re increases, while no mode transition is found for a lighter membrane at various Re and Ae . Finally, we examine the frequency characteristics of the leading edge vortex (LEV) and the trailing edge vortex (TEV) and compute the cross-correlation between the membrane deflection, the vortex shedding process and the surface pressure difference fluctuation. Based on the aeroelastic modal analysis, we suggest a feedback loop for flexible membrane wings undergoing synchronized self-excited vibration.

† Email address for correspondence: li.guojun@u.nus.edu

‡ Email address for correspondence: rjaiman@mech.ubc.ca

Key words: flow-structure interactions, aeroelastic mode transition, self-excited vibration, swimming/flying

Nomenclature

Ae	aeroelastic number, $E^s h/0.5\rho^f U_\infty^2 c$
AR	aspect ratio, b^2/S
\mathbf{A}_k	global amplitude spectrum
b	span
c	chord
\mathcal{C}	global spatial mode sequence
C_D	drag normalized by $\rho^f U_\infty^2 S/2$
\mathbf{c}_k	Fourier complex coefficient
C_L	lift normalized by $\rho^f U_\infty^2 S/2$
C_{my}	moment about the y -axis normalized by $\rho^f U_\infty^2 S c/2$
C_N	normal force normalized by $\rho^f U_\infty^2 S/2$
C_p	pressure normalized by $\rho^f U_\infty^2/2$
C_{pd}	pressure difference normalized by $\rho^f U_\infty^2/2$
C_{Power}	aerodynamic power normalized by $\rho^f U_\infty^3 c b/2$
C_{sp}	membrane surface pressure normalized by $\rho^f U_\infty^2/2$
C_T	tension normalized by $\rho^f U_\infty^2 S/2$
d	width of the supporting frame section
E^s	Young's modulus
\mathbf{E}	global spatial mode energy sequence
e_k	mode energy spectrum
f	frequency
f_k	discretized frequency
f_s	sampling frequency
h	thickness
H^s	curvature of the deformed membrane
L_c	length of membrane in the freestream direction
L_i	length of monitoring line i
m^*	mass ratio
\mathbf{n}	outer normal to interface
p	pressure
r	radius of the support rob
Re	Reynolds number, $\rho^f U_\infty c/\mu^f$
R_{xy}	cross-correlation coefficient
S	wing planform area
s_k	global power spectrum
St	Strouhal number, $f c/U_\infty$
t	time
T	period
T^s	membrane tension
$\bar{\mathbf{u}}^f$	fluid velocity
\mathbf{x}	spatial coordinate
\mathbf{Y}	physical data
α	angle of attack
δ_n	membrane displacement normal to the chord
$\boldsymbol{\theta}_k$	global phase spectrum
κ_n	wavenumber

μ^f	dynamic viscosity
ρ^f	density of fluid
ρ^s	density of structure
$\bar{\sigma}^f$	fluid stress tensor
τ	non-dimensional time shift
ω_n	radian frequency
ω_y	Y-vorticity
λ	wavelength
λ^s	membrane stretch ratio
$\overline{(\)}$	period-averaged value
$(\)'$	fluctuation component
$(\)_\infty$	freestream condition

1. Introduction

Fluid-structure interaction between a flexible membrane structure and the surrounding unsteady flow is ubiquitous in nature and engineering systems. During the past decades, morphing wings with elastic membrane components have received substantial attentions from the aerospace engineering community in the context of bio-inspired swimming/flying vehicles at the low Reynolds number regime ($Re < 10^5$) (Webster & Griffin 1962; Shyy et al. 1999; Bahlman et al. 2013). Flexible membrane wings may possess superior aerodynamic performance with improved lift-to-drag ratio, delayed stall and enhanced flight stability while maintaining light-weight structures, compared to conventional aircraft wings. In particular, the light-weight morphing membrane wing offers a possible solution for producing overall favourable flight efficiency and smooth adaptability in a gusty flow (Song et al. 2008). The dynamic interactions between flexible membranes and fluid flows can alter the wing configuration passively and excite particular aeroelastic modes through fluid-membrane coupling effect which can lead to flow-induced vibrations (FIVs) at certain conditions. The characteristics of different types of FIVs significantly affect the membrane performance and the aeroelastic instability of flexible membrane wings (Rojratsirikul et al. 2011; Sun et al. 2017). Due to the coupled nonlinear dynamical effects, the intertwined aeroelastic modes excited in the coupled system pose a serious difficulty with regard to the physical understanding for a wide range of conditions. There is a need for further understanding of the synchronized coupling between the vortex shedding and the flexible membrane and the mechanism of FIVs in flexible membrane wings. In the present study, we consider a 3D rectangular membrane wing with all fixed edges to identify the dominant aeroelastic modes from the coupled system and to establish a direct connection between the unsteady flow and the flexible membrane.

During fluid-membrane interaction (FMI), the phenomenon of FIV occurs by the strong coupling between the flexible membrane structure and the surrounding unsteady separated flow as well as the shed vortices. As illustrated in figure 1 (a), the perturbation induced by the pressure fluctuations travels backwards to enforce the elastic membrane to vibrate by leaving its static equilibrium position. These enforced travelling waves (TWs) interact with their boundary reflections (BRs) and give rise to a coupled self-excited vibration with intertwined modes. When the absorbed energy overcomes the net damping of the movable membrane, the structural responses are attracted by the limit cycle oscillation (LCO) via nonlinear constraints, yielding to a dynamic balanced

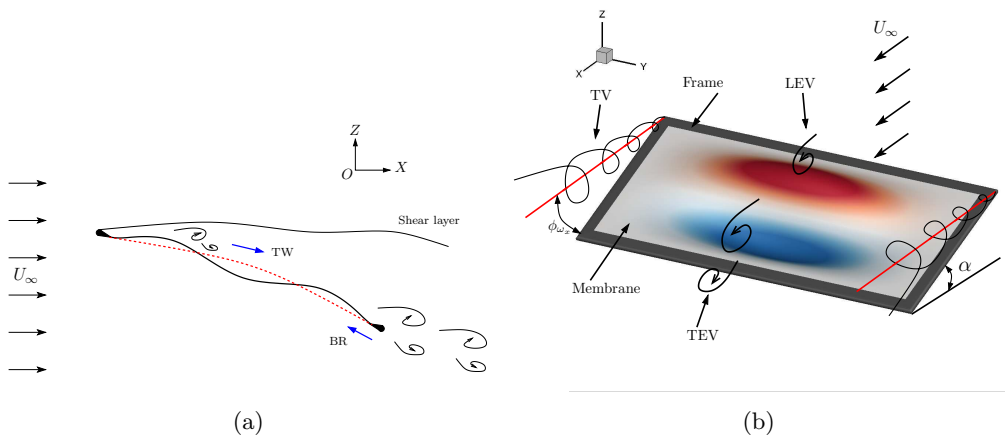


Figure 1: Flow past a flexible membrane wing: (a) schematic of fluid-membrane interaction, (b) illustration of membrane wing with free-stream velocity U_∞ and a given angle of attack α . While the red dash line (---) indicates the time-averaged membrane shape, the black solid line (—) represents the instantaneous membrane shape. ϕ_{ω_x} donates the angle between the membrane and the core of the tip vortex. The red and blue contours are the positive and negative membrane displacements, respectively.

state. It was found that the perturbation induced by the membrane vibration was able to improve the lift force via the fluid-membrane coupling effect, compared to the rigid wing with the same mean camber (Rojratsirikul *et al.* 2009; Gordnier 2009). Figure 1 (b) shows a schematic of the unsteady flow past a 3D rectangular membrane wing. From the perspective of the unsteady flow, the pressure distributions on the membrane surface and the induced wake structures behind the membrane wing are influenced by the static deformation or the dynamic vibrations with specific modes. The vibrational energy absorbed from the unsteady flow and the flow kinematic energy are redistributed through the FMI and it is mainly concentrated in several specific frequencies of the coupled fluid-membrane system (Serrano-Galiano *et al.* 2018). Particularly, the membrane resonance is excited as the vortex shedding frequency coincides with certain natural frequencies of the elastic membrane (Song *et al.* 2008).

Further recent studies based on experiments and numerical simulations suggested that the characteristics of FIV were strongly related to the membrane performance. Earlier investigations on FMI primarily focused on the mean dynamic responses of the flexible membrane exposed in the unsteady flow. However, the unsteady dynamic behaviours induced by the shear layer instability, rolled up separation and shed vortices depicted in figure 1 (a) play an important role in the membrane performance (Rojratsirikul *et al.* 2009; Serrano-Galiano *et al.* 2018). Song *et al.* (2008) examined the effects of aspect ratio, compliance and pre-strain values on the unsteady membrane dynamics for a low aspect ratio (LAR) wing in a wind tunnel experiment. The results indicated that the compliant wing produced larger lift forces and delayed stall, compared to its rigid counterpart. Secondary vortices induced by local separation at higher vibrational modes weakened the aerodynamic performance. Moreover, the FIVs in the coupled system were found to exhibit different characteristics for membranes with different geometries of the LE and TE (Arbós-Torrent *et al.* 2013; Serrano Galiano & Sandberg 2016), different excess lengths and pre-strain values (Rojratsirikul *et al.* 2010a) and at various flow conditions

(e.g. angle of attack and Reynolds number) (Rojratsirikul *et al.* 2009). Consequently, the flexible membrane wings showed a variety of flow performances related to different types of FIVs. In nature, bats are capable of dynamically changing the material properties via the miniature muscles and the biological tissues involved in the membrane organization and the high degree-of-freedom skeleton system according to the flight requirements as the membrane shapes and the flow conditions are fixed. Therefore, the material properties are also crucial to the membrane performances. However, few investigations on the effects of membrane material properties have been performed via wind tunnel experiments.

In relation to the FIV phenomenon, various vibrational modes and wake patterns are excited in the coupled system. Mode transition between different aeroelastic modes was observed as the angle of attack (AOA) changes (Song *et al.* 2008; Bleischwitz *et al.* 2015) or under forced pitching motion (Tregidgo *et al.* 2013). The reason for the mode transition phenomenon remains unclear and has not been systematically studied. Once the mode transition is triggered, the dominant modes might be fixed at a certain mode within a range of aeroelastic parameters. For example, a typical chord-wise second mode with varied vibrational frequencies was always observed for a two-dimensional (2D) membrane wing with the fixed ends when the membrane incidence exceeded the stall angle at different free-stream velocities (Rojratsirikul *et al.* 2009). Similar conclusions have been obtained in wind tunnel experiments for 3D membrane wings at high incidences (Rojratsirikul *et al.* 2010b; Tregidgo *et al.* 2011). Moreover, the occurrence of second mode was independent of the geometries at the leading and trailing edges (Arbós-Torrent *et al.* 2013). Tregidgo *et al.* (2011) found that the membrane vibrating in the second mode was related to the vortex lock-in behaviour of a rigid airfoil. The possible reason was attributed to the close coupling of the membrane oscillations and the particular vortex shedding process in the wake.

In parallel to experimental research, a substantial number of numerical simulations have been performed on flexible membrane wings using various methods. Numerical simulations can provide further insight into the evolution of membrane dynamics in a large parameter space without the restriction of membrane material properties and flow conditions in the experiments. Earlier relevant works focused on the one-dimensional (1D) linear elastic membrane model with the small deformation assumption in a potential flow (Newman 1987) or in a laminar flow (Smith & Shyy 1995) due to the limitation of the numerical models. The recently rapid development in computational fluid dynamics (CFD), computational structural dynamics (CSD) and fluid-structure coupling algorithms provided a practical and reliable way to investigate various nonlinear membrane dynamics with a wide range of aeroelastic parameters. Gordnier (2009) developed a high-fidelity computational simulation by coupling a sixth-order Navier-Stokes solver and a 1D nonlinear membrane solver to study the 2D fluid-membrane interaction at low Reynolds numbers. The effects of angle of attack, membrane rigidity, membrane pretension and Reynolds number on membrane dynamic responses have been investigated based on the proposed numerical simulation tool. The results confirmed the tight coupling between the membrane oscillations and the vortical structures in the wake, which was similar to the phenomena observed in the experiments (Song *et al.* 2008; Rojratsirikul *et al.* 2009). The evolutions of the nonlinear dynamic behaviours of a 2D membrane under periodic load (Sun & Zhang 2016) and the membrane with the perimeter reinforcement (Sun *et al.* 2017; Sun & Zhang 2017) have been studied systematically. The results indicated that the membrane dynamics was closely dependent on the initial conditions applied on the membrane wing and the material properties. Besides, the membrane inertia enlarged the AOA range of a 2D flexible membrane in a stable state in a laminar flow (Tiomkin & Raveh 2019). However, the study on the effect of membrane inertia focused on the FMI

at small AOA without obvious vortex structures. Only a handful of publications on 3D fully coupled aeroelastic analysis on a flexible membrane dynamics can be found in the literature. Recently, Yang *et al.* (2018) developed an aeroelastic solver based on the fully coupling between a high-fidelity fluid solver and a finite element structural solver and conducted a systematic validation for a 3D membrane dynamics. The numerical results achieved a good agreement with the experimental data (Rojratsirikul *et al.* 2009).

In previous studies on the membrane dynamics, the coupling between the membrane oscillations and the wake instabilities has been widely observed for different types of membrane wings. The investigation on the evolution of the induced spatio-temporal wake structures behind the membrane during FMI is lacking whereas the wake dynamics exhibits a strong relation with the force generation over a flexible structure (Dong *et al.* 2006; Andersen *et al.* 2017; Miyanawala & Jaiman 2019). Furthermore, the strong coupling effect excited and selected multiple modes of vibration and vortex shedding with different particular frequencies through an underlying mechanism of FMI. The mode transition and the vortex lock-in phenomena were observed over a wide range of aeroelastic parameters. The characteristics of excited vibrational modes, pressure fluctuations and wake structures play an important role in the membrane performances. Nevertheless, the interaction process between the membrane vibrations with overlapping structural modes and the vortex structures with various sizes enhances the complexity of the membrane dynamics. It is difficult to identify the dominant aeroelastic modes from the complex coupled system and properly connect the membrane vibrations and the unsteady flow. Although the traditional standard deviation analysis of the membrane deflection could reflect the dominant structural modal shape to some extent, the occasionally appearing modes or overlapping modes with small energies may be covered by the dominant modes, which makes them hard to be identified from the overall membrane vibrations. While plenty of investigations have been done to examine the physics of FMI through experimental and numerical approaches during the past decades, the understanding of the relationship between multiple excited modes and their corresponding flow patterns is still limited due to the complexity and overlap of flow-excited aeroelastic modes. Especially, the mechanism of the vortex lock-in and the mode transition related to the wake-membrane interaction is not yet fully understood.

The purpose of the present study is to identify the dominant aeroelastic modes from the coupled system and establish a direct connection between the flow-excited structural modes and the corresponding coherent flow structures as well as the induced wake patterns. Global mode decomposition techniques offer a practical way to extract the dominant aeroelastic modes and their harmonics from the overlapping dynamics, which have been recently used for the vorticity dynamics behind a circular cylinder (Zhang *et al.* 2014; Liu & Jaiman 2018; Miyanawala & Jaiman 2019). Different from the energy-ranked proper orthogonal decomposition (POD), the frequency-ranked Fourier mode decomposition (FMD) method (Ma *et al.* 2015; Bleischwitz *et al.* 2015; Serrano-Galiano *et al.* 2018) is capable of transferring the time-varying physical quantities into the frequency domain and extracting the decomposed fields at a selected characteristic frequency of the coupled system. He *et al.* (2019) performed a mode decomposition analysis for the fluid field of an airfoil connected with a flexible TE. The local fluid modes were successfully identified from the complex coupled system. This mode extraction strategy based on the FMD method can avoid the contamination of the concerned modes by the uncorrelated modes at undesired modal frequencies (Ma *et al.* 2015). The direct correspondence between the flow-excited structural modes and the coherent flow structures can be established via the FMD method at the selected characteristic

frequencies of interest. The contribution of individual modes to the overall membrane dynamics can be evaluated with the aid of FMD method.

In this study, we present novel physical insight and the underlying mechanism of how the unsteady turbulent flow interacts with the extensible 3D membrane to excite particular wake patterns and membrane vibrations at a moderate incidence. We employ the Fourier-decomposed modes of the coupled system to answer the following specific key questions that are relevant to the membrane aeroelasticity: (i) Which types of membrane vibrations and wake patterns are dominant during FMI and how do we identify these dominant aeroelastic modes? (ii) What is the intrinsic relationship between the flow features and the flow-induced structural mode? (iii) How do the aeroelastic parameters (e.g. mass ratio, Reynolds number and aeroelastic number) influence the aeroelastic instability for the FMI? (iv) What is the trigger factor of the mode transition and the vortex lock-in at various flow conditions? To address (i), we perform the global mode decomposition for the fluid-membrane coupling systems based on the FMD approach. Meanwhile, the contribution of the dominant mode and its harmonics to the overall membrane dynamics are calculated quantitatively to obtain the mode energy spectrum, which is utilized to identify the dominant aeroelastic modes at the energetic frequencies. We then study the relationship between the decomposed structural mode and its corresponding fluid mode with the same excitation frequency and explore an underlying mode selection mechanism for the coupled system. The effects of mass ratio m^* , Reynolds number Re and aeroelastic number Ae on the flow-excited membrane aeroelastic instability are studied through a series of coupled numerical simulations. We confirm the existence of the mode transition and the vortex lock-in phenomena from the mode transition map with the aid of the FMD method. The trigger factor of mode transition is further explored by examining the evolution of the inherent tension, the aerodynamic load and the characteristics of the energy done by the pressure difference. We finally study the coupling mechanism of the membrane oscillations and the wake instabilities and propose a feedback loop between the synchronization of the membrane vibration and the unsteady flow.

The remainder of this manuscript is organized as follows. In §2, we briefly introduce the governing equations for the fluid flow and the flexible elastic membrane. The description of the FMI problem and the validation of a 3D membrane with supporting rigid frame are conducted in §3. Section 4 presents the aeroelastic mode decomposition based on the FMD method and the underlying aeroelastic mode selection mechanism. A systematic analysis of the flow-excited membrane instability as a function of mass ratio, Reynolds number and aeroelastic number is studied and the mode transition as well as its trigger factor is presented in §5. A feedback loop of fluid-membrane coupling mechanisms is described in §6. In §7, the main conclusions of the aeroelastic instability in the coupled system are summarized.

2. Numerical methodology

2.1. Coupled fluid-structure formulation

The governing equations for the incompressible unsteady viscous flow with an arbitrary Lagrangian-Eulerian (ALE) reference frame are discretized using the stabilized Petrov-Galerkin variational formulation. The generalized- α method is utilized to integrate the ALE flow solution in the time domain and it can ensure unconditionally stable and second-order accuracy for linear dynamics problems. The motion equations for a flexible structure are discretized using the standard Galerkin finite element method. The

kinematic joints are considered as constraints on the displacement field. A partitioned iterative coupling algorithm is adopted to integrate the fluid equations and the multibody structural equations and a typical predictor-corrector scheme is used to solve the coupled aeroelastic governing equations. The velocity and traction continuity along the coupling interface with non-matching meshes is satisfied in the aeroelastic coupling procedure. An efficient interpolation scheme based on the compactly-supported radial-basis function (RBF) method is implemented to exchange coupling data through the aeroelastic interface and update meshes in the fluid domain. A recently developed nonlinear interface force correction (NIFC) scheme (Jaiman *et al.* 2016) is utilized to correct the fluid forces at each iterative step to avoid the numerical instability caused by significant added mass effect. The fluid-multibody structure interaction equations and the variational partitioned formulation for the FMI framework have been described in Li *et al.* (2019) in detail, which has been validated for an anisotropic flexible wing with supporting battens and covered membrane components (Li *et al.* 2019) and a 2D fluid-membrane interaction problem (Li *et al.* 2020).

2.2. Global Fourier mode decomposition

To identify and extract the global spatial modes at the specific frequency of interest, the Fourier mode decomposition (FMD) projects the entire physical data from the spatio-temporal domain to the spatio-frequency domain based on the discrete Fourier transform (DFT). In this section, the algorithm of FMD is introduced briefly and its application procedure to the FMI problems is presented.

The physical data $\mathbf{Y}(\mathbf{x}, t) \in \mathbb{R}^{M \times N}$ is collected from experiments and numerical simulations in a time-discrete way in most engineering problems. These data collected at M discretized spatial points \mathbf{x} and N sampling time constants is stored in an $M \times N$ matrix. The fluctuation components $\mathbf{Y}'(\mathbf{x}, t)$ reflect the perturbation in the time-varying global physical field $\mathbf{Y}(\mathbf{x}, t)$. Following the idea of Fourier series, the fluctuation function $\mathbf{Y}'(\mathbf{x}, t)$ can be written as a Fourier series in an exponential form:

$$\mathbf{Y}'(\mathbf{x}, t) = \sum_{k=0}^{N-1} \mathbf{c}_k(\mathbf{x}) e^{i \frac{2\pi k}{N} t} \quad (2.1)$$

The Fourier complex coefficient $\mathbf{c}_k(\mathbf{x}, f_k)$ at the discretized spatial point \mathbf{x} and the discretized frequency f_k is expressed as:

$$\mathbf{c}_k(\mathbf{x}, f_k) = \mathcal{F}(\mathbf{Y}'(\mathbf{x}, t)) = \frac{1}{N} \sum_{n=0}^{N-1} \mathbf{Y}'(\mathbf{x}, t) e^{-i \frac{2\pi k}{N} n} \quad (2.2)$$

In the global FMD analysis, we perform the discrete Fourier transform (DFT) to transfer the fluctuation function from the time domain to the frequency space $\mathbf{f} = [f_1, f_2, \dots, f_K] \in \mathbb{R}^{1 \times K}$ to obtain the global spatial mode sequence $\mathcal{C} = [\mathbf{c}_1(\mathbf{x}, f_1), \mathbf{c}_2(\mathbf{x}, f_2), \dots, \mathbf{c}_K(\mathbf{x}, f_K)] \in \mathbb{R}^{M \times K}$. The fast Fourier transform (FFT) algorithm is used to speed up the Fourier transform. The global spatial mode sequence \mathcal{C} consists of the decomposed spatial mode $\mathbf{c}_k(\mathbf{x}, f_k)$ at different frequencies f_k . The Fourier-transformed coefficients at each mesh point contain the information of the intensity and the initial phase of the spatial mode in the frequency domain. The global amplitude spectrum $\mathbf{A}_k(\mathbf{x}, f_k)$ and the global phase spectrum $\boldsymbol{\theta}_k(\mathbf{x}, f_k)$ can be written as:

$$\mathbf{A}_k(\mathbf{x}, f_k) = |\mathbf{c}_k(\mathbf{x}, f_k)| \quad \text{and} \quad \boldsymbol{\theta}_k(\mathbf{x}, f_k) = -\tan^{-1} \frac{\text{Im}(\mathbf{c}_k(\mathbf{x}, f_k))}{\text{Re}(\mathbf{c}_k(\mathbf{x}, f_k))} \quad (2.3)$$

In order to identify the dominant modes from the entire decomposed mode sequence, we calculate the sequence of the global power spectrum s_k and the mode energy spectrum e_k , which are expressed as

$$s_k = \|\mathbf{A}_k(\mathbf{x}, f_k)\| \quad \text{and} \quad e_k = \frac{s_k}{\sum_{k=1}^K s_k} \quad (2.4)$$

The mode energy spectrum e_k represents the contribution of individual spatial mode to the overall physical field. The real and imaginary parts of the spatial mode $\mathbf{c}_k(\mathbf{x}, f_k)$ show explicit physical significances for the spatial disturbance structures (modal shapes) and their intensity as well as initial phase difference. The dominant modes can be determined as the modes with most mode energies in the mode energy spectrum. Subsequently, these dominant modes are extracted from the frequency-ranked global mode sequence at the selected frequencies with relatively large mode energies. The global FMD method avoids the limitation of the traditional FFT analysis at a single point and provides a global view to reflect the correct dynamics of the entire physical field by containing the information of the decomposed modes at each spatial point (Ma *et al.* 2015). A summary of the FMD algorithm is presented in Algorithm 1.

ALGORITHM 1: FMD

Input: Storage of physical variables in the spatial field expressed as $\mathbf{Y}(\mathbf{x}, t) \in \mathbb{R}^{M \times N}$ (M , number of spatial mesh points; N , number of total time samples)

Output: Selected FMD modes $\mathcal{C} = [\mathbf{c}_1, \mathbf{c}_2, \dots, \mathbf{c}_K]$ and mode energies $\mathbf{E} = [e_1, e_2, \dots, e_K]$

(i) Extract the fluctuation physical variable matrix from time-varying global physical field: $\mathbf{Y}'(\mathbf{x}, t) = \mathbf{Y}(\mathbf{x}, t) - \overline{\mathbf{Y}}(\mathbf{x}, t)$

(ii) Calculate the global Fourier coefficients $\mathbf{c}_k(\mathbf{x}, f_k)$ by applying FFT approach

(iii) Find the mode energy e_k for its corresponding spatial mode

(iv) Determine the dominant spatial modes by detecting the peaks of the mode energy distributions as a function of frequency

Before we perform the FMD analysis of the FMI problem, there are several pre-processing steps to be completed. We first collect the time-varying physical variables of interest both in fluid and structural domains at each discretized mesh point with a sampling frequency of f_s . Considering the deformation of the flexible membrane under aerodynamic load, the positions of the body-fitted fluid mesh are updated by following the motion of the membrane at each iterative step in the developed FMI framework. In the present study, the physical field is decomposed via FMD method at fixed mesh points. We perform the interpolation for the collected physical variables from the moving fluid and structural meshes to the fixed reference mesh based on a RBF interpolation method. Subsequently, all the physical data is stored in a snapshot way for FMD analysis. The global FMD method is utilized to decompose the fluid and structural physical fields into frequency-ranked spatial modes based on (2.2). The primary advantage of the global FMD analysis is to establish correct correspondences of the decomposed fluid and structural Fourier modes by choosing the modes in both domains at the same selected frequency. This approach avoids the drawbacks of energy-ranked POD modes, that is, the decomposed fluid modes cannot be linked with the structural modes directly due to the multiple frequency contents in the modes. Another advantage of the FMD method is that it allows to extract the spatial modes with relatively small mode energies at frequencies of interest. Benefiting from the superiority of FMD, it is helpful to build an intrinsic relationship between the flow-induced vibrations and the coherent flow structures to

Parameters	Value	Description
b	137.5 mm	Span length
c	68.75 mm	Chord length
AR	2	Aspect ratio
U_∞	5.0 m/s	Free-stream velocity
α	$5^\circ \sim 25^\circ$	Angle of attack
ρ^f	1.21 kg/m ³	Fluid density
Re	24300	Reynolds number
h	0.2 mm	Thickness
E^s	2.2 MPa	Young's modulus
ρ^s	1000 kg/m ³	Membrane density
m^*	2.4	Mass ratio
Ae	423.14	aeroelastic number

Table 1: Aeroelastic simulation parameters for a flexible rectangular membrane wing

reveal the physical mechanism of FMI because of the explicit physical interpretation of the FMD results.

3. Numerical set-up and verification

3.1. Problem definition

In this section, we provide an overview of the FMI simulation set-up for a 3D rectangular flexible membrane wing immersed in a viscous incompressible fluid flow. The 3D wing consists of a latex rubber membrane sheet and a rectangular stainless steel frame. The thin membrane component has a thickness of $h = 0.2$ mm. The Young's modulus of the latex rubber is $E^s = 2.2$ MPa and its material density is $\rho^s = 1000$ kg/m³. The wing with an aspect ratio of 2 has a chord length of $c = 68.75$ mm. The membrane wing geometry and the information of the support frame section are displayed in figure 2 (a). The width of the supporting frame section is $d = 5$ mm and the diameter of the support rod is $2r = 2$ mm. Three key non-dimensional aeroelastic parameters, namely aeroelastic number Ae , mass ratio m^* and Reynolds number Re , govern the nonlinear dynamic responses of the flexible membrane aerofoils (Gordnier 2009), which are given as

$$Ae = \frac{E^s h}{\frac{1}{2} \rho^f U_\infty^2 c}, \quad m^* = \frac{\rho^s h}{\rho^f c}, \quad Re = \frac{\rho^f U_\infty c}{\mu^f} \quad (3.1)$$

where ρ^f represents the air density, U_∞ is the free-stream velocity and μ^f denotes the dynamic viscosity of the air.

The air load is calculated by integrating the surface traction taking into account the first layer of elements on the membrane surface. The instantaneous lift, drag and normal force coefficients are defined as

$$C_L = \frac{1}{\frac{1}{2} \rho^f U_\infty^2 S} \int_\Gamma (\bar{\boldsymbol{\sigma}}^f \cdot \mathbf{n}) \cdot \mathbf{n}_z d\Gamma \quad (3.2)$$

$$C_D = \frac{1}{\frac{1}{2} \rho^f U_\infty^2 S} \int_\Gamma (\bar{\boldsymbol{\sigma}}^f \cdot \mathbf{n}) \cdot \mathbf{n}_x d\Gamma \quad (3.3)$$

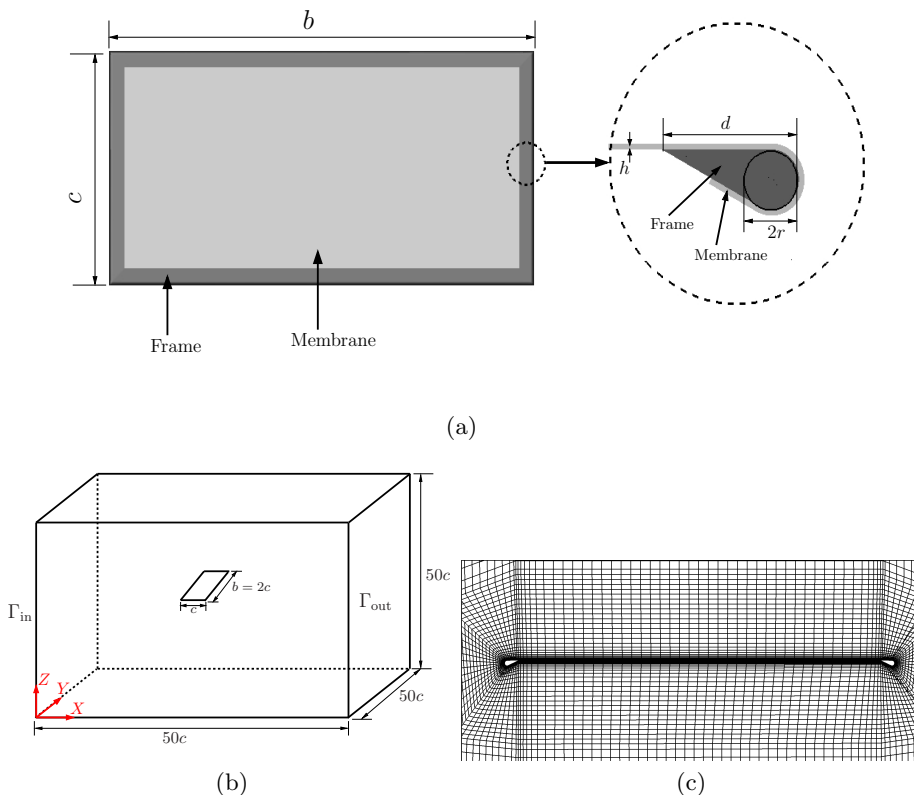


Figure 2: Three-dimensional computational set-up for fluid-membrane interaction: (a) membrane wing geometry and section of support frame, (b) schematic diagram of the computational domain and the boundary conditions and (c) representative mesh distribution in (Y,Z) -plane in the fluid domain.

$$C_N = \frac{1}{\frac{1}{2}\rho^f U_\infty^2 S} \int_{\Gamma} (\bar{\boldsymbol{\sigma}}^f \cdot \mathbf{n}) \cdot \mathbf{n}_c d\Gamma \quad (3.4)$$

where \mathbf{n}_x and \mathbf{n}_z are the Cartesian components of the unit normal \mathbf{n} to the membrane surface and \mathbf{n}_c is the unit normal to the chord line. $\bar{\boldsymbol{\sigma}}^f$ is the fluid stress tensor with Γ being the surface boundary of the membrane. The pressure coefficient is defined as

$$C_p = \frac{p - p_\infty}{\frac{1}{2}\rho^f U_\infty^2} \quad (3.5)$$

where p and p_∞ are the pressure at the concerned point and the pressure at the far-field, respectively.

A sketch of the three-dimensional computational domain used for the fluid-membrane interaction problem is shown in figure 2(b). We set the same length of $50c$ for the distances between the side walls (Γ_{slip}) on top and bottom as well as these on both sides and the distance between inlet (Γ_{in}) and outlet (Γ_{out}) boundaries. A uniform flow velocity $\bar{\mathbf{u}}^f = (u^f, v^f, w^f)$ is set at the inlet boundary Γ_{in} for the computational domain. The boundary condition on the top, bottom and both sides boundaries (Γ_{slip}) is defined as the slip-wall boundary condition. We apply a traction-free boundary condition for the outlet

boundary Γ_{out} , where $\sigma_{xx} = \sigma_{yy} = \sigma_{zx} = 0$. A no-slip boundary condition is applied on the membrane wing surface.

3.2. Mesh convergence and verification

Three different meshes namely M1, M2 and M3 are conducted to perform the mesh convergence study to determine a proper mesh resolution for the numerical simulation of the 3D flexible membrane wing. The 3D computational fluid domain is discretized by unstructured finite element mesh which consists of 341 821, 823 864 and 1 304 282 eight-node brick elements, respectively. The stretching ratio ($\Delta y_{j+1}/\Delta y_j$) for the mesh in boundary layer is set as 1.25 to keep y^+ less than 1.0. We choose a non-dimensional time step of $\Delta t U_\infty/c$ of 0.0364 in the simulations. Figure 2(c) presents the space mesh distribution along the wing span-wise direction in the fluid domain. The structural model of this rectangular membrane wing includes the rigid body elements to model the rigid frame and the geometrically exact co-rotational shell elements to simulate the elastic membrane. The structural model is discretized by 160, 228 and 352 structured four-node rectangular finite elements, respectively. A clamped boundary condition with all fixed degrees of freedom is imposed on the rigid frame and the flexible membrane is attached to this frame with allowed elastic deformation.

In our simulation, the same parameters obtained from the wind tunnel experiments are set for both the fluid and structure domains, which are presented in table 1. The critical parameters considered for the mesh convergence study are $Re = 24300$, $U_\infty = 5$ m/s and $\alpha = 15^\circ$. Table 2 summarizes the aerodynamic force characteristics and the non-dimensional dominant vortex shedding frequency for the meshes M1, M2 and M3. The mesh convergence error in the brackets denotes the percentage difference with respect to the finest mesh M3. The maximum error between the numerical solutions computed for the meshes M2 and M3 is less than 3%. Therefore, mesh M2 is adequate for the numerical verification study.

The numerical formulation for the FMI problem has been validated for a 2D flexible membrane wing with fixed ends at a moderate Reynolds number (Li *et al.* 2020). To validate the coupled solver for the 3D rectangular membrane wing, the comparison of the aerodynamic forces and the maximum membrane deformation with the previous available data of Gordnier & Attar (2014) for the wing at $Re=24300$ and $\alpha = 10^\circ$ is presented in table 3. A reasonable agreement among the membrane responses is achieved. Furthermore, figure 3 plots the magnitude of time-averaged normalized membrane surface displacement and the time-averaged normal force coefficient difference between the flexible membrane wing and rigid wing for the rectangular wing with $U_\infty=5$ m/s at various AOAs, compared to the data obtained from the experiment (Rojratsirikul *et al.* 2011) and the numerical simulation (Gordnier & Attar 2014). It can be observed that the overall trends of the membrane deformation and the aerodynamic characteristics are well predicted. Further validation of the detailed flow features around the 3D membrane wing can be found in Li *et al.* (2020).

4. Aeroelastic mode decomposition and mode selection mechanism

To identify the dominant aeroelastic modes, the global mode decomposition method based on the FMD analysis is adopted to identify and extract dominant modes from the full physical field at several selected energetic frequencies. The decomposed modes of the rigid wing and the flexible membrane are compared to reveal the aeroelastic mode selection mechanism.

Mesh	M1	M2	M3
Structural elements	160	228	352
Fluid elements	341 821	823 864	1 304 282
Mean lift \overline{C}_L	0.9022 (0.49%)	0.8902 (0.85%)	0.8978
Mean drag \overline{C}_D	0.2289 (2.97%)	0.2346 (0.55%)	0.2359
r.m.s. lift fluctuation $C_L'^{rms}$	0.0788 (16.17%)	0.0928 (1.28%)	0.0940
r.m.s. drag fluctuation $C_D'^{rms}$	0.0289 (10.25%)	0.0313 (2.80%)	0.0322
Dominant shedding frequency St	0.9668 (2.70%)	0.9937 (0%)	0.9937

Table 2: Mesh convergence of a 3D rectangular flexible membrane wing at $Re=24300$ and $\alpha = 15^\circ$.

	\overline{C}_L	\overline{C}_D	$\ \bar{\mathbf{d}}\ _{\max}/c$
Present (M2)	0.7336	0.1277	0.03200
Gordnier & Attar (2014)	0.7231	0.1270	0.03046

Table 3: Numerical comparison against reference data of Gordnier & Attar (2014) at $Re=24300$ and $\alpha = 10^\circ$.

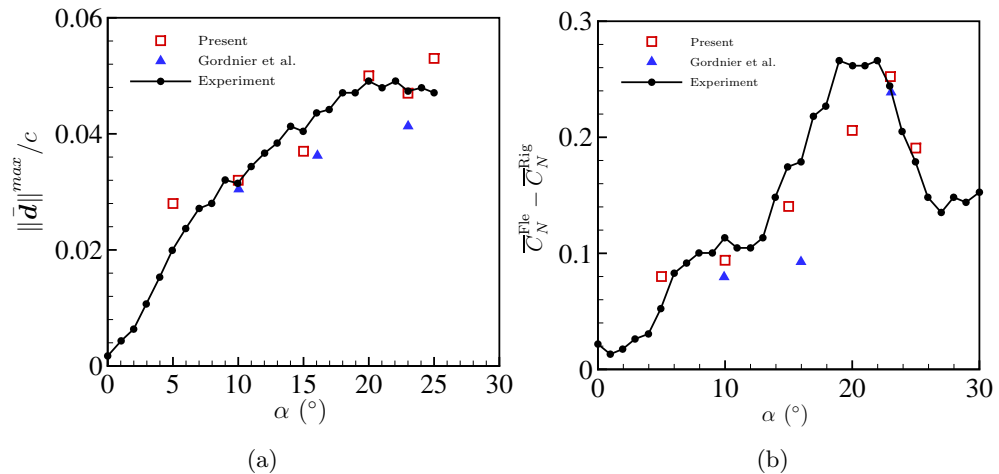


Figure 3: Flow past a 3D flexible membrane wing: (a) comparison of the magnitude of time-averaged normalized maximum membrane deformation ($\|\bar{\mathbf{d}}\|_{\max}/c$) for the present numerical simulation, experiment (Rojratsirikul *et al.* 2011) and numerical simulation (Gordnier & Attar 2014), (b) comparison of the time-averaged normal force coefficient difference ($\overline{C}_N^{\text{Fle}} - \overline{C}_N^{\text{Rig}}$) between the flexible membrane wing and rigid wing for the present numerical simulation, experiment (Rojratsirikul *et al.* 2011) and numerical simulation (Gordnier & Attar 2014).

Wing case	\overline{C}_L	\overline{C}_D	$\overline{C}_L/\overline{C}_D$
Rigid flat wing	0.7497	0.2171	3.4532
Flexible membrane	0.8902 (18.74% ↑)	0.2346 (8.06% ↑)	3.7945 (9.88% ↑)

Table 4: Comparison of aerodynamic characteristics for flow past the rigid flat wing and the flexible membrane at $Re=24300$ and $\alpha=15^\circ$.

4.1. Membrane aeroelasticity

Before proceeding to further investigation on the complex relationship between the flow-excited membrane vibration and the induced wake dynamics, we explore the effect of the membrane flexibility in the membrane aeroelasticity through a comparison of the flow characteristics between the rigid and flexible wings. Table 4 summarizes the aerodynamic characteristics for both wings. Compared to the rigid wing, the mean lift coefficient and the mean drag coefficient of the flexible membrane increases by 18.74% and 8.06%. As a result, the mean lift-to-drag ratio rises from 3.4532 to 3.7945 when flexibility is taken into account.

To gain further insight into how the unsteady flow interacts with the nonlinear structural motions of the membrane wing over time, the instantaneous flow features indicated by the streamlines around the rigid flat wing and the flexible membrane are presented in figure 4. A relatively large separated flow region is generated over almost the entire surface of the rigid flat wing. Compared to the flow fields of the rigid wing, it can be seen from figure 4 (b) that several main vortices with smaller sizes are formed on the upper surface of the membrane and the cores of these vortices are closer to the membrane surface. The LEV departs from the surface and convects downstream, then gradually sheds into the wake. During the vortex shedding process, pressure pulses are applied on the membrane surface as the vortices are released. The flexible membrane deforms up driven by the suction forces and the location of the maximum membrane deformation moves backwards by following the movement of the low pressure region. Thus, these shedding vortices are interacted with the elastic membrane at the most time instants directly to form membrane oscillations. Figure 5 presents the time-averaged membrane displacement and the standard deviation result. The maximum displacement is found near the centre of the membrane and it is almost symmetrical in the span-wise direction. It is observed from figure 5 (b) that the flexible membrane vibrates in a typical second mode at the moderate angle of attack.

The pressure distributions on the membrane surfaces and the oscillating flow field features around the wing are crucial to the aeroelasticity responses of the flexible membrane. To understand the effect of the membrane flexibility in FMI, we compare the time-averaged pressure difference between the upper and lower surfaces, the turbulent intensity and the local effective angle of attack α_{eff} for both wings shown in figure 6. The relatively larger suction force region is observed near the LE of the flexible membrane in figure 6 (a), compared to its rigid counterpart. The pressure is redistributed due to the cambered up wing shape and the negative pressure peaks at the LE are attributed to the LEVs. The shear layer fluctuations get closer to the flexible wing surface and become stronger near its LE. The high velocity fluctuations drive the flexible membrane to vibrate around its mean camber shape in an obvious second mode. The flexible membrane is stretched through deformation to balance the unsteady aerodynamic loads. Consequently, the local effective angle of attack at the LE changes with the vortex shedding process

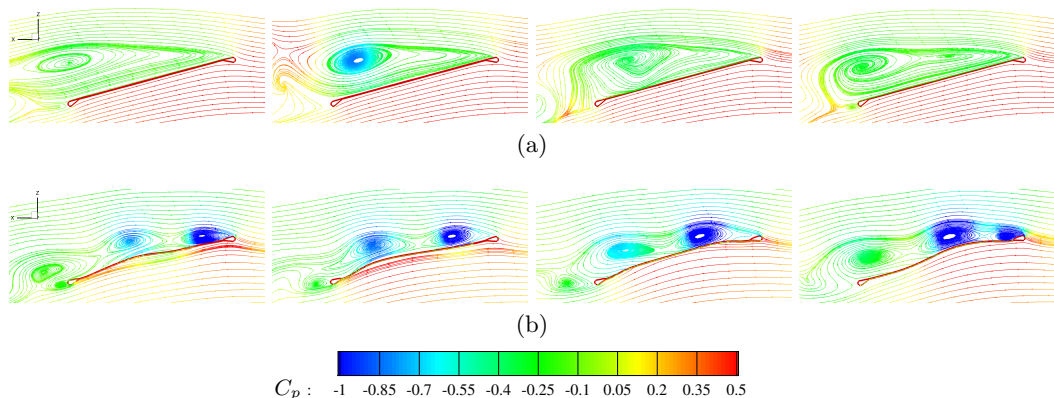


Figure 4: Instantaneous streamlines on the mid-span plane coloured by pressure coefficient within one cycle at $Re=24300$ and $\alpha=15^\circ$ for (a) rigid flat wing, (b) flexible membrane.

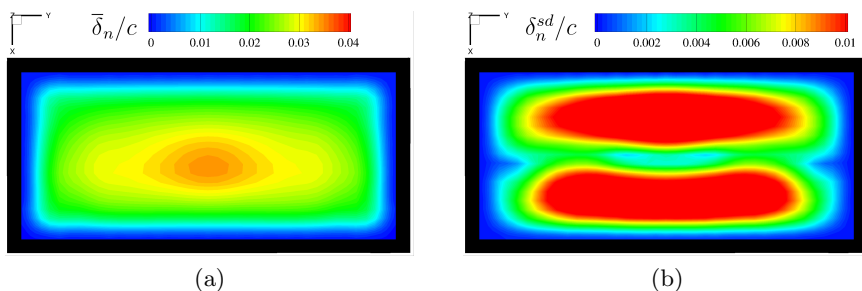


Figure 5: Flow past 3D flexible membrane wing at $Re=24300$ and $\alpha=15^\circ$: (a) time-averaged normalized membrane surface displacement normal to the chord $\bar{\delta}_n/c$ and (b) standard deviation analysis of normalized membrane displacement normal to the chord δ_n^{sd}/c .

during wing deformation. We extract the local effective angles of attack at the LE at the mid-span location for both wings, which is shown in figure 6 (c). The flexible wing possesses overall smaller effective angles of attack than the fixed angle of attack of 15° of the rigid wing within one cycle. The LEV on the membrane surface is allowed to attach longer on the flexible surface.

4.2. Aeroelastic mode decomposition and dominant mode identification

The flexible membrane is driven by the pressure pulsations over a wide range of frequencies to vibrate in complex behaviours. Figure 7 presents the aerodynamic force fluctuations and the instantaneous aeroelastic responses as well as the flow features around the flexible membrane within one full cycle at $\alpha = 15^\circ$ and $Re = 24300$. It can be seen from the displacement fluctuations that the flexible membrane shows an obvious chord-wise second mode at the non-dimensional time instants of $t/T = 0, 0.4$ and 1 . Furthermore, some fuzzy high-order modes are observed at $t/T = 0.2$ and 0.8 . Thus, the membrane oscillations appear to include an overlap of several modal shapes finally. The apparent wake structures with different flow scales are excited during FMI. Hence, it is difficult to identify the dominant membrane modal shapes from the overlapping vibrations with multiple modes. Meanwhile, the dominant vortical structures are hard

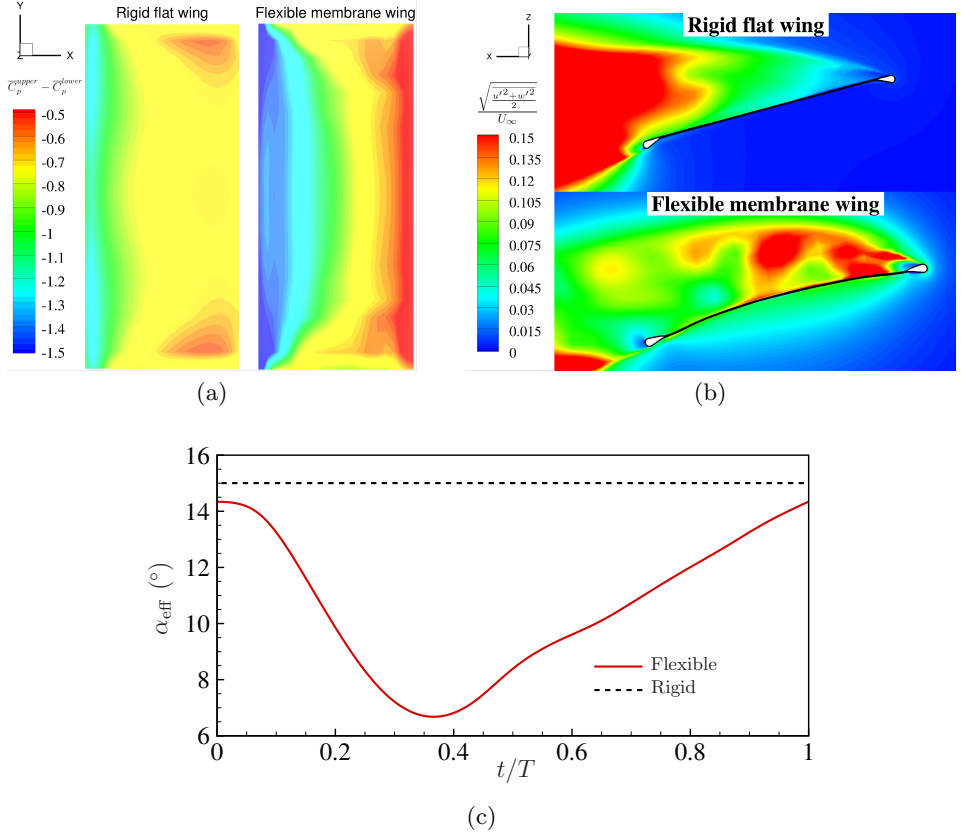


Figure 6: Comparison of flow features between the rigid flat wing and the flexible membrane wing at $Re=24300$ and $\alpha=15^\circ$: (a) time-averaged pressure coefficient difference between the upper surface and the lower surface, (b) turbulent intensity on the mid-span plane and (c) local effective angles of attack at the LE on the mid-span location.

to isolate from the flow fields and correlate with the corresponding membrane modes directly due to the diversity of obvious vortex scales and spatial flow structures. This poses a serious challenge to fully understand the FMI mechanism in the unsteady viscous flow.

The FMD method is employed to decompose the complex spatio-temporal membrane aeroelastic responses and fluid fields with 512 time-varying samples into frequency-ranked Fourier modes. The mode energies of the decomposed aeroelastic modes calculated from (2.4) are used to identify the dominant frequencies of the aeroelastic modes with most energies. Then, the dominant modes are extracted from the whole responses at the selected frequencies to build a direct connection between the structural modes and the flow modes. We decompose the aeroelastic responses of the flexible membrane wing at $Re=24300$ and $\alpha=15^\circ$ to demonstrate how the FMD works for the FMI problems. Two obvious frequency peaks at $St = 0.99$ and 1.96 are observed in the computed mode energy spectra for the decomposition of the membrane surface displacement, the pressure field and the Y -vorticity field in figure 8 (a). It is noticed that the energetic frequencies are consistent for the decomposed structural and flow Fourier modes. This indicates the membrane vibrations and the flow fluctuations are excited at the same frequencies with a strong coupling effect. The decomposed aeroelastic modes coloured by the real part of

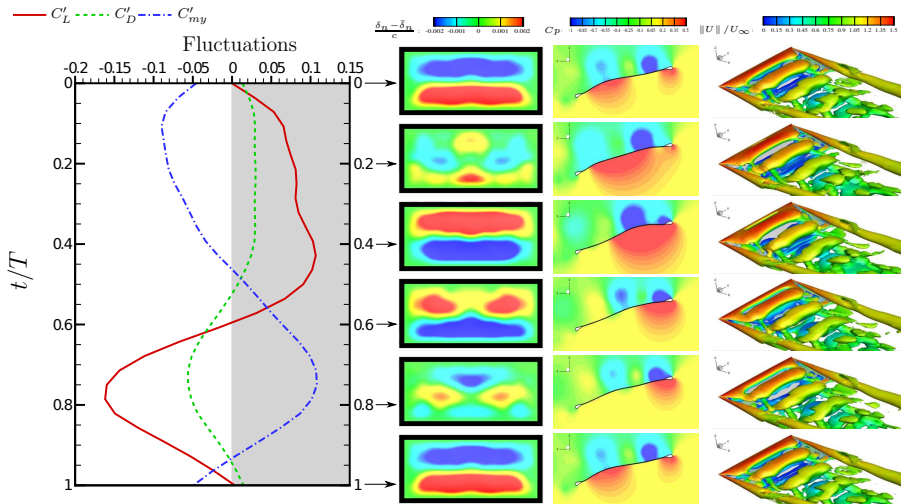


Figure 7: Instantaneous membrane dynamics at six time instants within one full cycle at $Re=24300$ and $\alpha=15^\circ$. The mean values are removed from the full unsteady aerodynamic forces to present the lift coefficient fluctuation C'_L , the drag coefficient fluctuation C'_D and the moment coefficient fluctuation C'_{my} . The red and blue colours indicate upward deformation and downward deformation away from the mean membrane shape in the membrane displacement fluctuation contour. The pressure distributions around the membrane are extracted on the mid-span plane. The wake structures are plotted by the instantaneous iso-surfaces of $Q(= -\frac{1}{2} \frac{\partial u_i^f}{\partial x_j} \frac{\partial u_j^f}{\partial x_i})$ value. Iso-surfaces of non-dimensional $Q^+ \equiv Q(c/U_\infty)^2 = 0.5$ are coloured by the normalized velocity magnitude $\|U\|/U_\infty$.

the Fourier transform coefficients based on the displacements and the pressure difference distributions of the membrane surface at the selected dominant frequency of $St = 0.99$ and 1.96 are plotted in figure 8 (b-e), respectively. We notice that a typical chord-wise second mode is excited at $St = 0.99$ and a high-order mode both in the chord-wise and span-wise directions is observed at a higher frequency of $St = 1.96$. Except for the decomposed surface pressure modal shapes near the LE, the overall modes present similar modal shapes as the decomposed surface displacement modes at both frequencies.

To study the spatial flow structures induced by the membrane vibration, we decompose the spatial pressure and Y -vorticity fields on the mid-span plane via the FMD method. The real part $Re(\mathcal{F}(C_p - \bar{C}_p))$ and the amplitude $|\mathcal{F}(C_p - \bar{C}_p)|$ of the decomposed pressure fluctuation fields at the non-dimensional frequency of $St = 0.99$ corresponding to the chord-wise second mode are shown in figure 9 (a,b), respectively. The real part of the transformed coefficients reflects the spatial structures of the mode. The amplitude represents the intensity distributions of the decomposed physical variables. Two small-scale pressure fluctuation regions are observed near the LE on the upper membrane surface. These pressure fluctuations are mainly caused by the local shear layer instability and the rolled up vortices at the LE in figure 10 (a). Two larger pressure fluctuation regions on the upper surface are generated during the periodic LEV shedding process along the path in figure 10 (a). The pressure wavelength on the lower surface is almost one membrane chord length. From the amplitude contour of the decomposed pressure field in figure 9 (b), the large-scale pressure pulsations with high values are noticed on

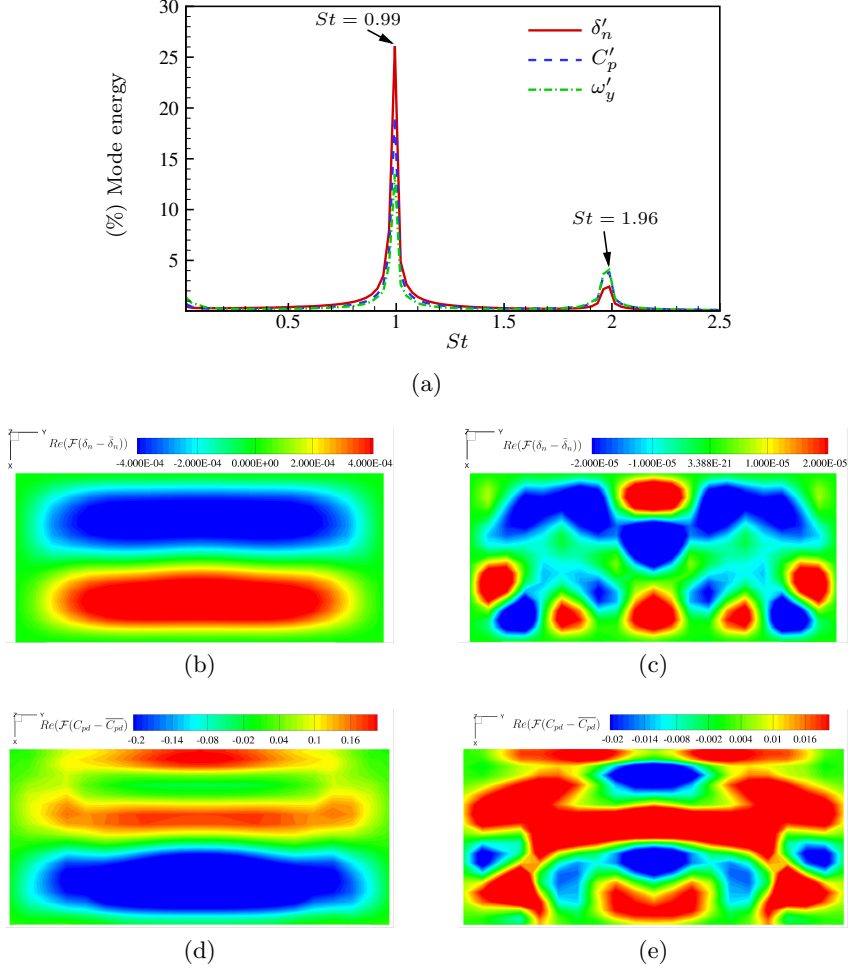


Figure 8: Aeroelastic mode decomposition of 3D flexible membrane at $Re=24300$ and $\alpha=15^\circ$: (a) mode energy spectra of the surface displacement fluctuations, the pressure coefficient fluctuations and the Y -vorticity fluctuations based on the FMD analysis; the decomposed membrane displacement modes at $St =$ (b) 0.99 and (c) 1.96 and the surface pressure difference modes at $St =$ (d) 0.99 and (e) 1.96.

the upper surface. The severe vorticity fluctuations are mainly formed at the periodic vortex shedding regions near the LE and TE in figure 10 (b).

As the increase of the non-dimensional frequency to $St = 1.96$ with the high-order mode, the pressure wavelength and the flow scales become smaller. The high-intensity pressure pulsations still keep close to the membrane surface in figure 9 (d). However, the amplitude values in this region are far less than those at $St = 0.99$ due to the weaker mode energy of the high-order mode. Meanwhile, the small-scale vortices originating from the LE move backwards to merge with the TEVs behind the membrane in figure 10 (c). It can be observed from figure 10 (d) that the high-intensity vorticity fluctuation region shrinks and the amplitude values in this region reduce, compared to the decomposed vorticity field at the dominant frequency of $St = 0.99$.

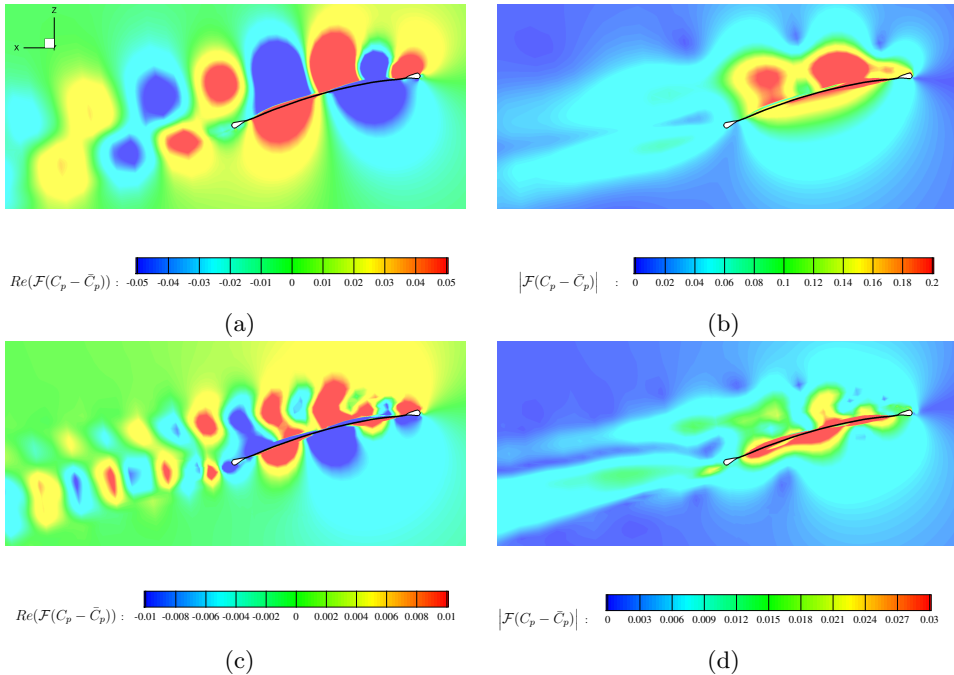


Figure 9: Aeroelastic mode decomposition of 3D flexible membrane at $Re=24300$ and $\alpha=15^\circ$: contours of the real part (a,c) and the amplitude (b,d) of the Fourier transform coefficients of the pressure coefficient fluctuation field corresponding to the non-dimensional frequency of $St =$ (a,b) 0.99 and (c,d) 1.96.

4.3. Aeroelastic mode selection mechanism

From the observation of the aeroelastic responses and the spatial flow structures of the flexible membrane, the intertwined modes are excited through FMI. The results indicate that flexibility plays an important role in selecting particular aeroelastic modes via an underlying mechanism. To understand the underlying aeroelastic mode selection mechanism, we analyse the decomposed fluid fields of the rigid wing with 512 time-varying samples and compare with those of the flexible wing. Figure 11 presents the frequency spectra of the global mode energy for the surface pressure coefficient fluctuation and the spatial Y -vorticity fluctuation of the rigid flat wing and the flexible membrane. The surface pressure fluctuation indicates the external pulsation acting on the surface and the vorticity fluctuation represents the vortex shedding process in the flow space around the wings. The frequency spectra of the rigid wing show almost continuous frequency contents within $St \in [0, 0.6]$. The non-dimensional frequency of the dominant surface pressure mode is around 0.0805 and the most energetic modal frequency of the spatial vorticity changes to 0.5102. Different from the modal frequency spectra of the fluid fields for the rigid flat wing, the mode energies of the flexible wing are redistributed into several specifically discrete frequencies of the coupled system via the flexibility effect. The frequency contents of the flexible wing between the decomposed surface pressure and the spatial vorticity are highly consistent. The most energetic aeroelastic mode is excited at the non-dimensional frequency of $St = 0.99$. The rest of the modal frequencies with the obvious energy concentration are noticed at the harmonics of the dominant mode.

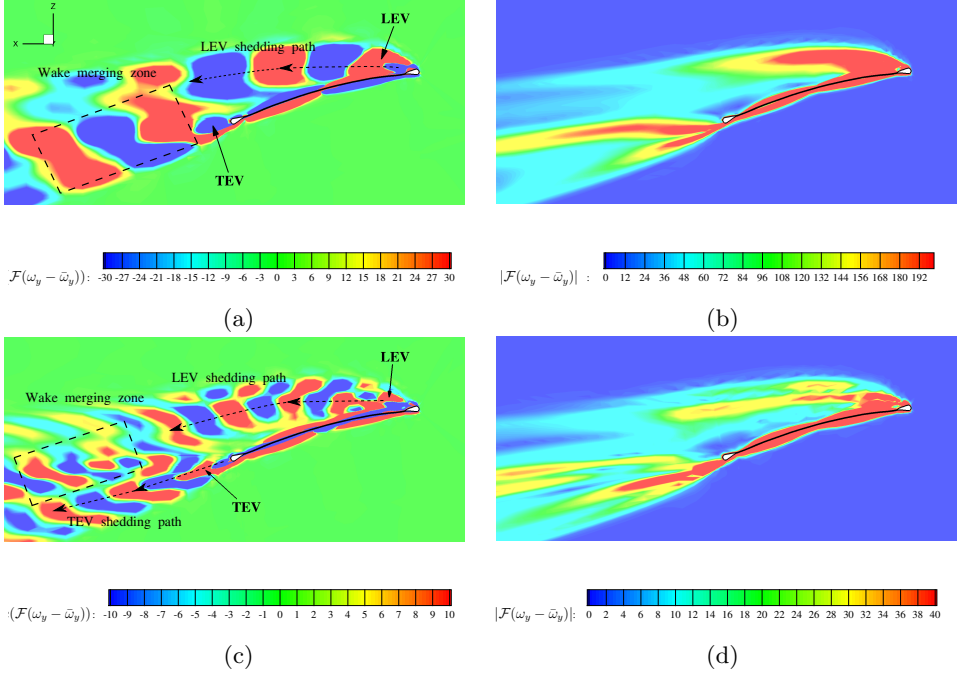


Figure 10: Aeroelastic mode decomposition of 3D flexible membrane at $Re=24300$ and $\alpha=15^\circ$: contours of the real part (a,c) and the amplitude (b,d) of the Fourier transform coefficients of the Y -vorticity fluctuation field corresponding to the non-dimensional frequency of $St = (a,b) 0.99$ and (c,d) 1.96.

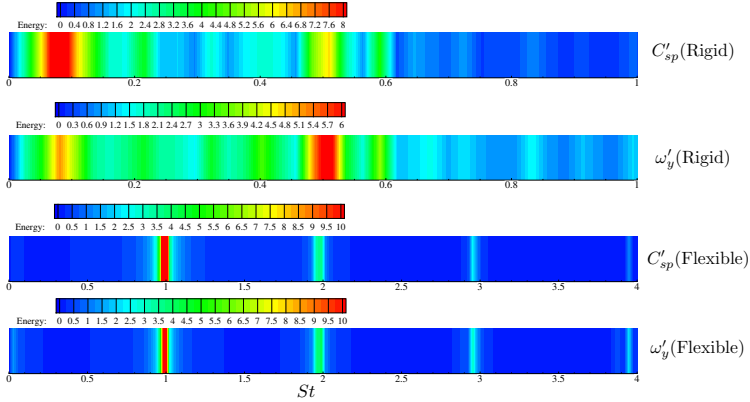


Figure 11: Comparison of global mode energy spectra of the fluctuations of the surface pressure coefficient fluctuation and the spatial Y -vorticity fluctuation between the rigid flat wing and the flexible membrane at $Re=24300$ and $\alpha=15^\circ$.

For further comparison of the effect of the membrane flexibility on the flow features, the decomposed pressure and Y -vorticity modes of the rigid flat wing are extracted at two most energetic frequencies of $St = 0.0805$ and 0.5102 . The real part and the amplitude of the Fourier-transformed coefficients based on the FMD method are presented in figure 12 and figure 13, respectively. At $St = 0.0805$, it is observed from figure 12 (a,b) that

the pressure fluctuates severely on the surface near the LE and in the proximity of the TE. The fluctuations in this region are mainly caused by the excited vortex structures observed from the contour of the real part of the decomposed vorticity mode in figure 13 (a). A high amplitude of the decomposed vorticity mode is observed on almost the entire surface in figure 13 (b).

At $St = 0.5102$, the pressure wavelength observed from the real part of the transformed pressure field in figure 12 (c) becomes shorter than that at the lower frequency of $St = 0.0805$. Furthermore, the high-intensity pressure fluctuation region is only noticed near the TE of the wing in figure 12 (d). Noticed from the real part and the amplitude of the decomposed vorticity field in figure 13 (c,d), the vortices are mainly formed in the proximity of the TE and then shed into the wake periodically with a higher frequency of $St = 0.5102$. It can be inferred from the decomposed pressure and vorticity modes that the pressure fluctuations at the TE are attributed to the wake shedding behind the wing.

It can be concluded from the comparison of the flow features between the flexible wing and the rigid flat wing in §4.1 that the rolled up vortices with smaller sizes get closer to the flexible membrane surface due to the cambered up wing shape and the membrane vibration. The flow energy is redistributed into several specific frequencies through the strong coupling effect between the unsteady flow and the flexible membrane. The excitation frequencies of the flow field are almost the same as those of the membrane vibration, which indicates a frequency synchronization between them. The vortex shedding patterns of the flexible membrane are significantly affected due to the flexibility effect based on the global mode decomposition analysis for both wings. The rolled up vortex at the LE travels along the LEV shedding path shown in figure 10 (a,c). Then it merges with the TEVs in the proximity of the TE to periodically shed into the wake with the corresponding frequencies excited in the coupled system. It is worth noting that this vortex shedding process causes the pressure around the membrane to oscillate at a specific wavelength. More importantly, the pressure fluctuation region with high values becomes closer to the membrane surface, compared to the pressure field of the rigid flat wing. Consequently, the flexible membrane is driven by the pressure pulsations acting on the surface and vibrates in particular modal shapes. The direct connection between the decomposed surface vibration modes and the surface pressure modes in figure 8 confirms that there is an inherent mechanism to select aeroelastic modes in the coupled system.

To gain a deeper insight into the characteristics of the membrane vibration and the external pressure pulsation, we next evaluate the wavelength of each decomposed surface pressure and membrane vibration mode based on the wavenumber-frequency spectrum. Membrane vibration and pressure pulsation can be regarded as a waveform signal in essence. A simple 1D homogeneous linearised equation is employed to approximately describe the waveform signal. The wave equation with fixed ends can be given as

$$\rho^s \frac{\partial^2 \delta_n(x, t)}{\partial t^2} = T^s \frac{\partial^2 \delta_n(x, t)}{\partial x^2} \quad (4.1)$$

Boundary condition: $\delta_n(x = 0, t) = 0$ and $\delta_n(x = c, t) = 0$

where ρ^s represents the density and $\delta_n(x, t)$ denotes the vertical deflection. A general solution of (4.1) for a wave with fixed ends can be expressed as the superposition of

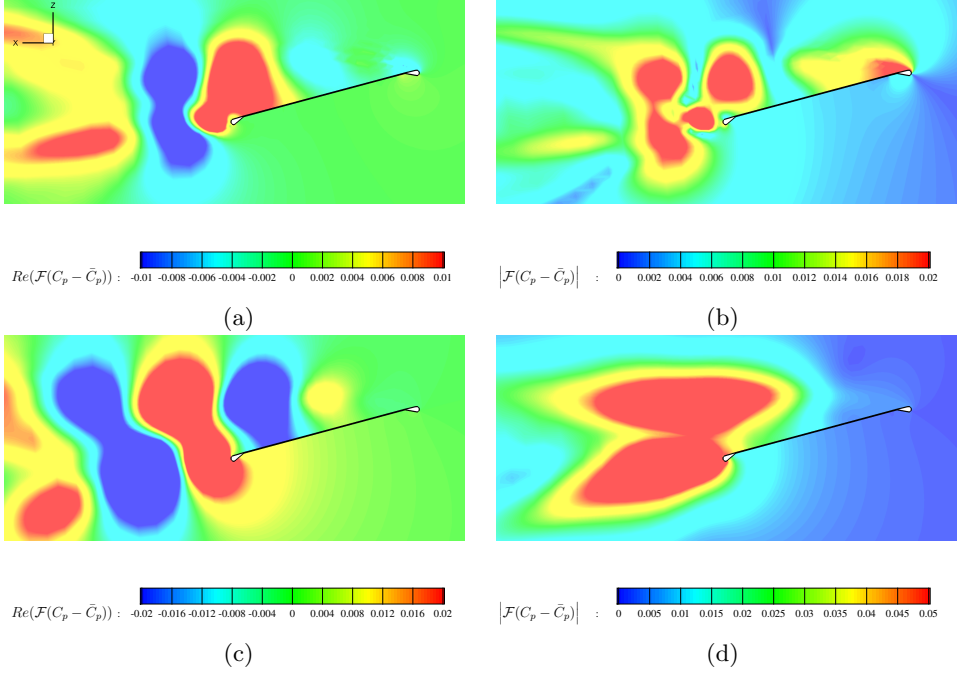


Figure 12: Aeroelastic mode decomposition of 3D rigid wing at $Re=24300$ and $\alpha=15^\circ$: contours of the real part (a,c) and the amplitude (b,d) of the Fourier transform coefficients of the pressure coefficient fluctuation field corresponding to the non-dimensional frequency of $St =$ (a,b) 0.0805 and (c,d) 0.5102.

particular solutions given as (Kinsler *et al.* 1999; Graff 2012)

$$\begin{aligned}
 \delta_n(x, t) &= \sum_{n=1}^{\infty} [a_n \cos(\kappa_n x - \omega_n t) - a_n \cos(\kappa_n x + \omega_n t) \\
 &+ b_n \sin(\kappa_n x - \omega_n t) + b_n \sin(\kappa_n x + \omega_n t)] \\
 &= \sum_{n=1}^{\infty} [2a_n \sin(\omega_n t) + 2b_n \cos(\omega_n t)] \sin(\kappa_n x)
 \end{aligned} \tag{4.2}$$

where κ_n is the wavenumber and ω_n represents the radian frequency. a_n and b_n are the decomposition coefficients, respectively. This expression presents the procedure of decomposing a given wave-like response into the defined basic sinusoidal function $\sin(\kappa_n x)$ with different wavelengths. The wavelength corresponding to a specific vibrational frequency can be computed based on the double Fourier transform (DFT). The wavenumber-frequency spectrum displays the relationship between the wavenumber and the frequency of a waveform and it offers the detailed information of how the wave travels. This spectrum is calculated based on the DFT to convert the physical signals $y(x, t)$ into both wavenumber and frequency space. The equation of DFT is expressed as

$$\mathcal{F}(y(x, t))(f, \lambda) = \frac{1}{N} \frac{1}{M} \sum_{t=0}^{N-1} \sum_{x=0}^{M-1} y(x, t) e^{-i2\pi ft} e^{-i\frac{2\pi}{\lambda} x} \tag{4.3}$$

where λ is the wavelength and f represents the frequency. $\mathcal{F}(y(x, t))(f, \lambda)$ is the double Fourier-transformed coefficient.

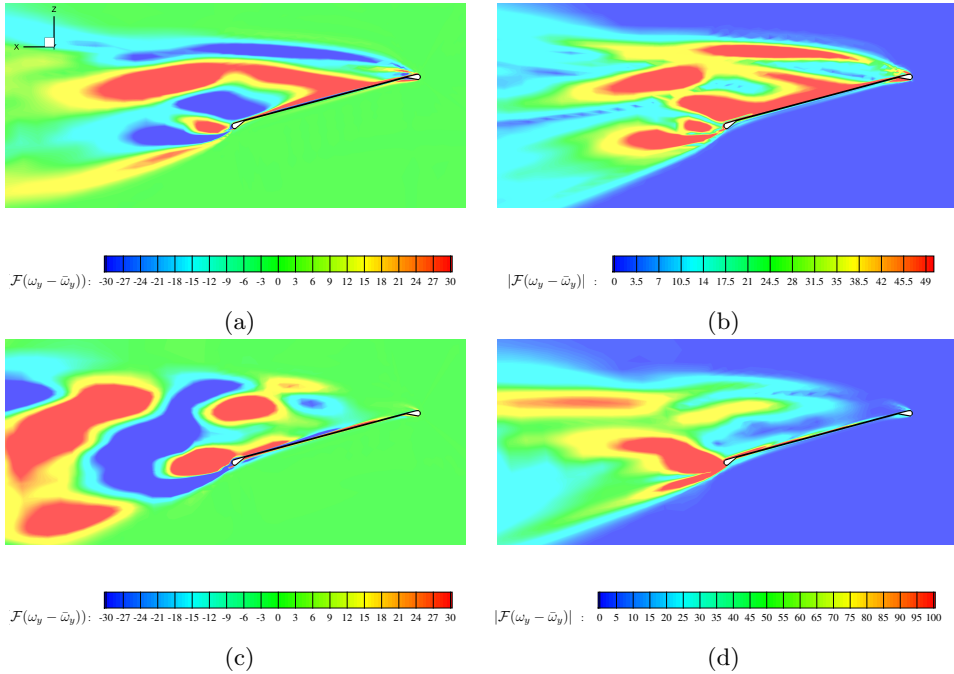


Figure 13: Aeroelastic mode decomposition of 3D rigid wing at $Re=24300$ and $\alpha=15^\circ$: contours of the real part (a,c) and the amplitude (b,d) of the Fourier transform coefficients of the Y -vorticity fluctuation field corresponding to the non-dimensional frequency of $St =$ (a,b) 0.0805 and (c,d) 0.5102.

Based on the analysis of the decomposed membrane vibration mode, the decomposed pressure mode and the decomposed vorticity mode, we build a direct relationship between the membrane dynamics, the pressure excitation and the vortex structure via the modes of interest at the same coupled frequency. We further connect the membrane vibration and the surface pressure excitation through the wavenumber-frequency spectrum to reveal the aeroelastic mode selection mechanism. We extract the time-varying membrane vibration and surface pressure signals at 256 equispaced points at the mid-span location along the chord-wise direction of the membrane wing for 512 non-dimensional time instants. These data samples are stored in a time-space matrix. The mean values are removed from the full signals and the fluctuations of the analysed signals are mapped into frequency-wavenumber space through the DFT. The wavenumber-frequency diagrams of the membrane deflection fluctuations and the pressure difference fluctuations are plotted in figure 14. These 2D diagrams are coloured by the amplitude of the double Fourier transformed coefficients of the analysed signal functions. The x -axis is the wavenumber of the unit chord length c/λ and the y -axis indicates as the Strouhal number $St = fc/U_\infty$.

The dominant frequency of $St = 0.99$ and its harmonics with obviously concentrated energies are observed in both diagrams. The excitation frequency contents are consistent for the membrane vibration and the pressure pulsation. In the wavenumber-frequency spectrum of the membrane deflection fluctuations (figure 14 (a)), the wavelength of the membrane vibration at $St = 0.99$ is approximately one chord length of the wing. The wavelength reduces to 0.66 of the wing chord length at $St = 1.96$ for the high-order mode. Different from the pure modal shape of the structural vibration, the decomposed pressure modes in figure 8 (b) show shorter wavelengths due to the existence of the rolled up LEVs

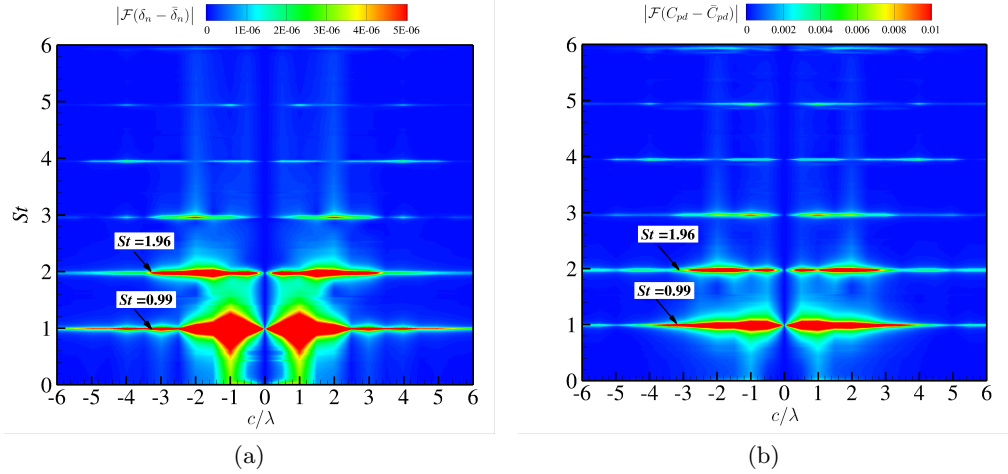


Figure 14: Wavenumber-frequency spectra of: (a) membrane deflection fluctuations and (b) pressure coefficient difference fluctuations along the flexible membrane at the mid-span location.

in the proximity of the LE. Although the LEVs moving backwards induce a small portion of the pressure fluctuations at the LE, the remaining modal shapes of the pressure field exhibit similar characteristics to the membrane vibration. The predominant wavelength of the surface pressure fluctuations at $St = 0.99$ is 0.9 of the wing chord length c . For the high-order mode at $St = 1.96$, the pressure wavelength becomes smaller to $0.625c$.

In summary, the aeroelastic mode is selected through the strong coupling between the pressure excitations and the membrane vibrations, which possess similar modal shape distributions with a comparable wavelength at the same excitation frequency. The external pressure pulsations are caused by the formation, movement and reattachment of the separated flow. Hence, the wavelength and the frequency of the pressure fluctuations are related to the scale and the shedding frequency of the vortex passing through the membrane surface. As the external pressure pulsations drive the flexible membrane to vibrate at the several specific frequencies, the rolled up vortex travels through the membrane surface and periodically shed into the wake with the same excitation frequencies under the disturbance of the enforced membrane vibration. Eventually, the unsteady flow and the membrane vibration enter a strong coupling state and the frequency synchronization to select the particular aeroelastic modes. The mode decomposition analysis of flexible membranes at other angles of attack shown in Appendix A also confirms this aeroelastic mode selection mechanism. Once we establish the direct connection between the unsteady flow and the membrane vibration with the aid of FMD analysis, it is helpful to explore the fluid-membrane coupling mechanism over a wide range of parameter space. In the following sections, we then investigate the evolution of the aeroelastic instability as a function of mass ratio m^* , Reynolds number Re and aeroelastic number Ae at a moderate AOA of 15° . The FMD analysis is used to identify the dominant modes and their mode energies to provide further insight into the FIVs and the aeroelastic instability of the flexible membrane.

5. Flow-excited membrane instability and mode transition

The relevant aeroelastic parameters, such as mass ratio m^* , Reynolds number Re and aeroelastic number Ae , play important roles in the membrane aeroelastic instability. In this section, we firstly explore the evolution of membrane aeroelastic instability as a function of the structure-to-fluid mass ratio m^* . Three distinct vibrational modes are identified at various mass ratios. Then, the mode transition map is presented based on the FMD analysis of the aeroelastic responses to investigate the transition between different dynamic modes. We further examine the trigger factor of the mode transition and the mode synchronization between the unsteady flow and the flexible membrane by increasing membrane inertia, changing Reynolds number and releasing Young's modulus.

5.1. The role of mass ratio in membrane instability

The mass ratio of the bio-inspired membrane wings with thin structures varies over a wide range because of the diversity of flying species and the capability of dynamically changing membrane material properties during flight. Different membrane dynamics and aerodynamic characteristics are observed for various types of membrane wings. Previous research works (Gurugubelli & Jaiman 2015) demonstrated that mass ratio affected the unsteady flapping modes of a flexible structure dramatically. Hence, it is essential to investigate how mass ratio affects the membrane instability. In this study, we focus on the flexible membrane at a moderate AOA slightly below the stall angle. For the first time, we systematically investigate the evolution of the aeroelastic instability as a function of m^* for the flexible membrane undergoing strong coupling with the passing-by vortical structures. We present the vibration responses of an elastic 3D membrane for $m^* \in [0.36, 24]$ with a moderate angle of attack of $\alpha = 15^\circ$ at $Re = 24300$ and $Ae = 423.14$. The evolution of the membrane instability at various mass ratios and the mode transition mechanism are studied in detail in the following sections.

Flexible membrane loses its stability via static divergence or unsteady interaction dynamics. The membrane finally achieves a new stable state in one of the two distinct stability regimes, namely (a) deformed-steady state (DSS) for $0 < m^* \leq 1.2$ and (b) dynamic balance state (DBS) for $1.2 < m^* \leq 24$. The above membrane stability regimes are classified based on the full-body profiles at the mid-span location in figure 15. In the DSS regime for $0 < m^* \leq 1.2$, it can be observed from figure 15 (a,b) that the flexible membrane has a stable cambered up shape and no obvious oscillation is noticed in this regime. By increasing m^* value, the flexible membrane tends to leave the static equilibrium position and oscillates around its mean position in specific modal shapes. We further identify three distinct vibrational modes in the DBS regime from the full-body profile responses, namely (i) asymmetric chord-wise second mode for $1.2 < m^* \leq 3.6$, (ii) transitional mode for $3.6 < m^* \leq 4.8$ and (iii) symmetric chord-wise first mode for $4.8 < m^* \leq 24$. Figure 15 (c,d) shows the full-body profiles for $m^* = 1.65$ and 2.4 within one completed oscillation cycle. The flexible membrane vibrates about the cambered up mean shape in a typical chord-wise second mode. We notice that the instantaneous membrane profile in this mode oscillates only on one side of the undeformed wing shape in an asymmetric manner. It is noteworthy that the flexible membrane tends to vibrate on both sides while the mean membrane shape becomes closer to the undeformed wing for $m^* \in (3.6, 4.8]$. The predominant vibrational mode transitions from the second mode to the first mode within this mass ratio range. When the inertial effect becomes stronger, the flexible membrane performs relatively large amplitude oscillations predominantly in the symmetric first mode for $m^* = 7.2, 14.4$ and 24 in figure 15 (g,h,i). Moreover, the membrane responses show a mean membrane shape with almost zero camber.

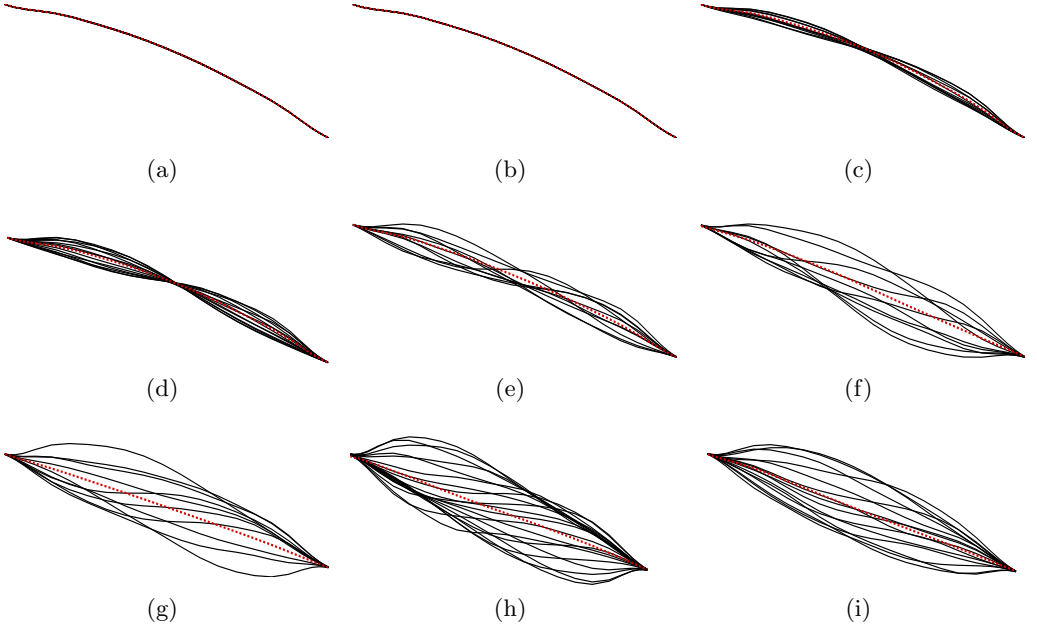


Figure 15: Full-body responses of 3D flexible membrane wing at mid-span location at $\alpha = 15^\circ$ and $Re = 24300$ for $m^* =$ (a) 0.48, (b) 1.2, (c) 1.65, (d) 2.4, (e) 3.6, (f) 4.8, (g) 7.2, (h) 14.4 and (i) 24. (---) denotes the time-averaged membrane shape.

To further investigate the role of mass ratio in the membrane aeroelastic instability, we plot the mean and root-mean-squared (r.m.s.) fluctuation values of the aerodynamic characteristics and the membrane displacements at various m^* in figure 16. The DSS regime is coloured by white. In this regime, the mean lift coefficient, drag coefficient and lift-to-drag ratio remain almost constant for the values of 0.747, 0.2032 and 3.6752, respectively. Meanwhile, the flexible membrane wing has a stable camber with a nearly constant maximum normalized membrane deflection about 0.0365. Thus, the aerodynamic characteristics and the membrane responses have no obvious oscillation and the r.m.s. values of the fluctuations are negligible. The results indicate that the flexible membrane reaches a new stable equilibrium position via the static deformation at relatively low mass ratios and shows non-oscillating aerodynamic forces in the DSS regime.

By increasing m^* to 1.2, the flexible membrane tends to leave its static equilibrium position and finally enters the DBS by obtaining LCO. The aeroelastic response of the flexible membrane in the DBS with grey colour are further divided into three types of vibrational modes with dash lines in figure 16. The time-averaged lift and drag coefficients and the r.m.s. values of their fluctuations increase sharply as m^* grows up to 2.4, and then the mean forces reach a flat with a slight change before the membrane vibration turns into the transitional mode. Consequently, the lift-to-drag ratio shows a similar trend as the lift and drag forces. The maximum mean membrane deflection is almost reduced to 2/3 of the deflection in the DSS continuously as m^* increases from 1.2 to 3.6. Meanwhile, the flexible membrane vibrates more severely in a chord-wise second mode.

The contribution of the chord-wise first mode to the overall membrane vibration response becomes stronger, and gradually tends to be comparable to the contribution

of the second mode as the further increase of m^* to 4.8. The membrane behaves a transitional mode between the asymmetric second mode and the symmetric first mode in this regime. The maximum mean lift coefficient of 0.8948 is observed at $m^* = 3.6$ in figure 16 (a) when the flexible membrane starts to enter the transitional mode. Then, the mean lift coefficient reduces slightly to 0.8689 at $m^* = 4.8$. Meanwhile, the mean drag coefficient remains about 0.234 in the transitional mode. As a result, the optimal mean lift-to-drag ratio of 3.8142 is achieved at $m^* = 3.6$, and then it is reduced by 2.31% at $m^* = 4.8$. It can be seen from figure 16 (a,b) that the lift and drag coefficients perform larger oscillation amplitudes when the inertial effect becomes stronger. Since the flexible membrane is prone to vibrate symmetrically on both sides of the undeformed wing, the wing camber becomes smaller, resulting in a continuous decrease of the mean membrane deformation shown in figure 16 (d). Moreover, the membrane wing exhibits greater amplitude oscillations as m^* increases.

The chord-wise first mode tends to dominate the full-body profile responses when m^* is greater than 4.8. For $m^* \in (4.8, 24]$ in figure 16 (a), the mean lift coefficient reduces slightly from 0.8689 to 0.8545 until $m^* = 8.4$, and then it almost keeps a constant number about 0.865 at a relatively larger m^* . The oscillation amplitude of the lift coefficient fluctuations constantly grows up and it reaches the maximum value of 0.3017 at $m^* = 9.6$. Subsequently, the amplitude is gradually reduced by 22.24% at $m^* = 24$. It can be observed from figure 16 (b) that the mean drag coefficient jumps to a plain at $m^* = 6.0$ and it keeps constant around 0.247 finally as m^* further increases. Meanwhile, the r.m.s. value of the drag coefficient fluctuation firstly increases and then drops to 0.0494 at $m^* = 24$. The change of the lift and drag coefficients leads to a continuous reduction of the mean lift-to-drag from 3.72 to 3.50 within $m^* \in (4.8, 9.6]$ shown in figure 16 (c). An approximately constant value of the mean lift-to-drag about 3.5 is achieved at relatively large mass ratios for $9.6 \leq m^* \leq 24$. It is noticed from figure 15 (f-i) that the mean membrane profile gradually approaches to the undeformed wing when m^* increases from 4.8 to 24. Consequently, the maximum mean membrane deflection is reduced by 47.25% in this regime. Meanwhile, the maximum amplitude of the vibration fluctuation rises to 0.004089 at $m^* = 24$. There is a common phenomenon that both the mean values and the r.m.s. fluctuation values of the aerodynamic forces and the membrane deformation almost tend to be constant when $m^* \geq 14.4$.

To further investigate how various mass ratios affect the membrane instability, we compare the instantaneous flow features within one cycle around the flexible membrane and the turbulent intensity on the mid-span plane for the membrane aeroelasticity in different regimes in figure 17 and figure 18, respectively. We choose the aeroelastic responses of the membrane at $m^* = 1.2$ for the DSS and $m^* = 2.4, 3.6$ and 14.4 for the second mode, the transitional mode and the first mode in the DBS regime, separately. For $m^* = 1.2$ in figure 17 (a), a large region of separated flow is observed on almost the whole upper surface of the membrane. The large-scale vortex here is assembled with the TEV to form a vortex pair behind the membrane, which is similar to a typical von Karman vortex shedding process behind a bluff body. It is noticed from figure 18 (a) that the high-intensity flow fluctuation region is far away from the membrane surface. Thus, the flexible membrane can remain the DSS with no obvious vibration because the fluctuation of the surrounding flow is very weak.

As the inertial effect becomes stronger, the flexible membrane vibrates in one of the specific modes within the DBS regime. The membrane vibration in the second mode excites the shear layer separation in the proximity of the LE causing it to roll up and to form a chain of vortices convecting downstream at $m^* = 2.4$ shown in figure 17 (b), compared to the flow features in the DSS. Meanwhile, the separated shear layer

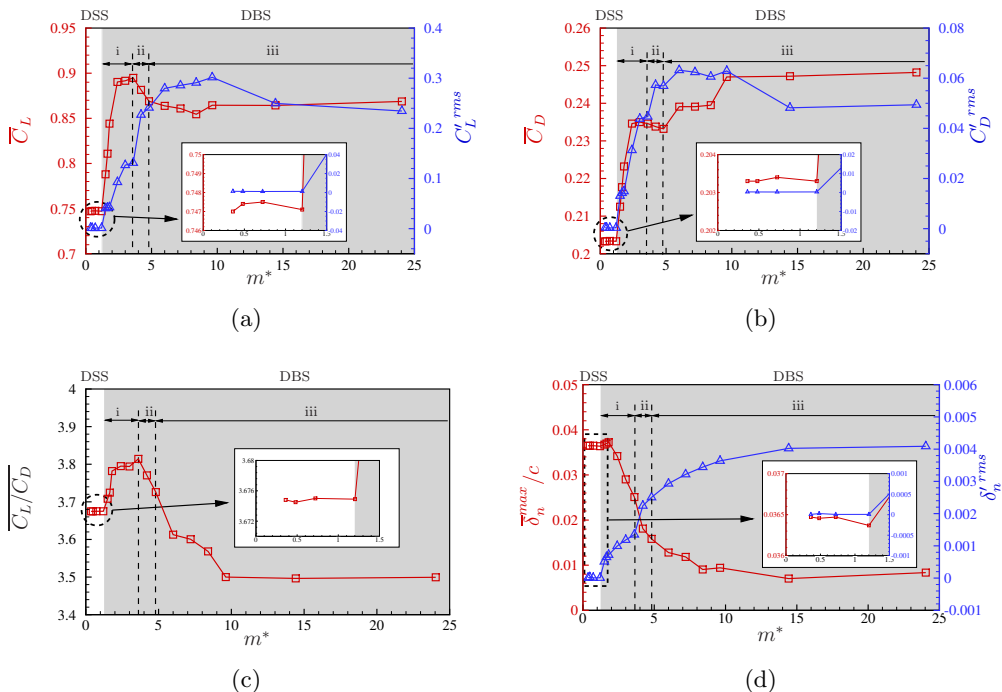


Figure 16: Evolution of 3D membrane dynamics as a function of m^* : (a) mean lift coefficient and r.m.s. lift coefficient fluctuation, (b) mean drag coefficient and r.m.s. drag coefficient fluctuation, (c) mean lift-to-drag ratio and (d) the maximum time-averaged normalized membrane deflection and r.m.s. membrane deflection fluctuation.

gets closer to the membrane surface and becomes more energetic as observed in figure 18 (b). In turn, the fluctuating flow induced by the vortex shedding process drives the flexible membrane to leave the deformed-steady position and to obtain a new dynamic balance state finally. It is observed from figure 17 (c) that the vortex shedding pattern is changed by containing low frequency contents due to the occasionally occurring first mode component in the transitional regime at $m^* = 3.6$. In figure 18 (c), the separated shear layer still keeps close to the surface and the fluctuating intensity becomes stronger than that at $m^* = 2.4$. Thus, this phenomenon leads to larger amplitude oscillations of the aerodynamic forces and the membrane deformation. The obvious first vibrational mode is observed in figure 17 (d) at $m^* = 14.4$. In this mode, only one apparent large-scale vortex detaches from the surface and sheds into the wake in a completed oscillation period, which is synchronized with the first membrane vibration mode. Furthermore, the fluctuation of the surrounding flow becomes more serious with a larger turbulent intensity close to the surface shown in figure 18 (d). As a result, this highly unstable flow results in a large-amplitude first mode of the flexible membrane vibrating around the undeformed wing almost symmetrically.

5.2. Mode transition

From the results in the previous section, we observe that the flexible membrane loses its static stability and achieves a new dynamic balance state at a critical mass ratio of $m^* = 1.2$. In the DBS regime, the predominant vibrational mode transitions from the second mode to the first mode as the mass ratio increases. This mode transition

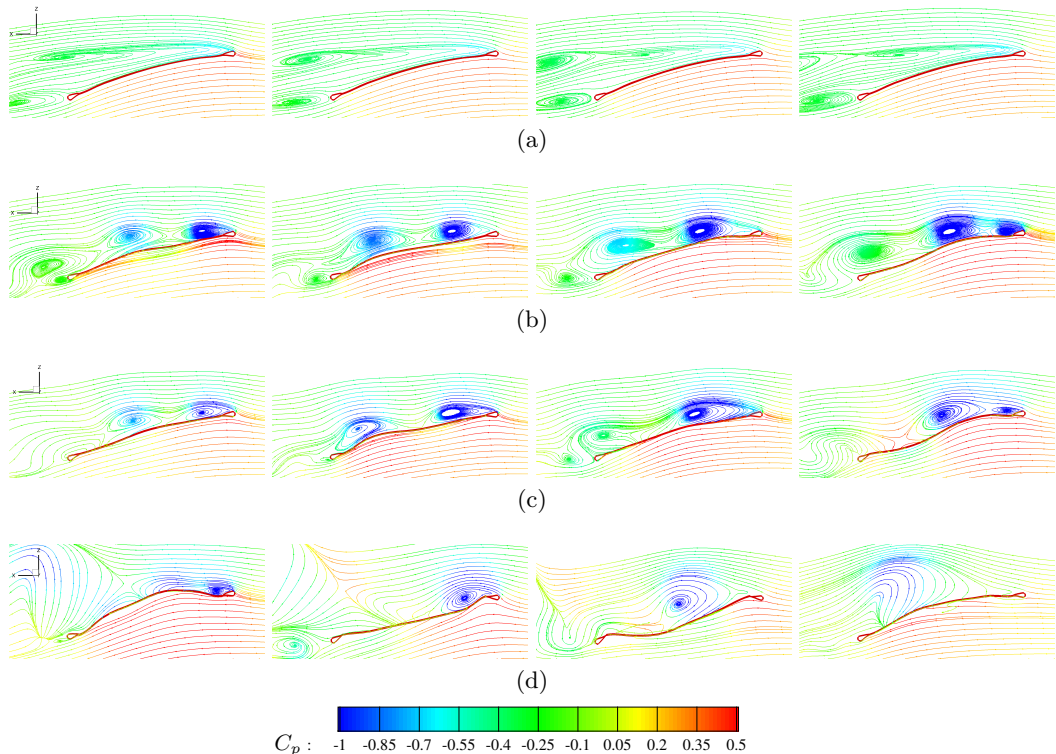


Figure 17: Instantaneous streamlines of 3D flexible membrane wing on the mid-span plane coloured by pressure coefficient within one cycle at $\alpha = 15^\circ$ and $Re = 24300$ for (a) $m^* = 1.2$ in DSS, (b) $m^* = 2.4$ in asymmetric second mode, (c) $m^* = 3.6$ in transitional mode and (d) $m^* = 14.4$ in symmetric first mode.

phenomenon is influenced by the changes of the aeroelastic parameters related to FMI. However, the trigger factor of the mode transition needs further investigation. In this section, we plot the mode transition map obtained based on the FMD analysis of the aeroelastic responses. The mode frequencies and the mode energies are presented as a function of mass ratio m^* . We then explore the trigger factor for the mode transition.

5.2.1. Mode transition map

The global FMD analysis performed in §4 demonstrates that this mode decomposition method allows isolating the energetic aeroelastic modes from the overlapping membrane dynamics. Meanwhile, the dominant frequencies and the contribution of each mode to the overall aeroelastic responses can be identified. The mode transition phenomenon is observed from the full-body profile responses in the dynamic regime as mass ratio changes in §5.1. To get a deeper insight into the mode transition phenomenon, we present the mode transition map including the mode energy spectra, the mode frequencies of the obvious membrane modes and the mode energies for $m^* \in [1.5, 24]$ in the DBS regime in figure 19 with the aid of FMD analysis.

The contour of the mode energy spectra shown in figure 19 (a) is coloured by the mode energy computed from (2.4). We observe that the flexible membrane firstly vibrates in a dominant non-dimensional frequency about 1.0, and then the dominant frequency gradually switches to half its original frequency content through the transitional region

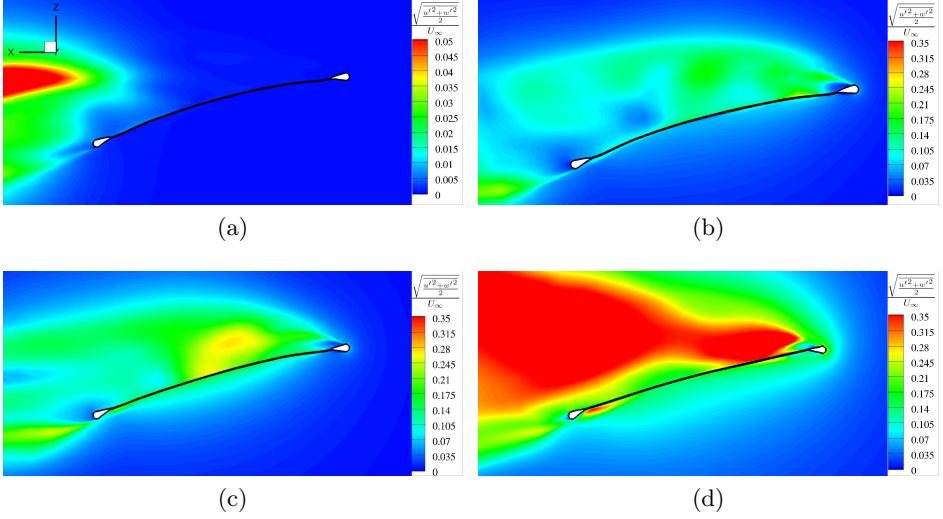


Figure 18: Turbulent intensity of 3D flexible membrane wing at mid-span location at $\alpha = 15^\circ$ and $Re = 24300$ for (a) $m^* = 1.2$ in DSS, (b) $m^* = 2.4$ in asymmetric second mode, (c) $m^* = 3.6$ in transitional mode and (d) $m^* = 14.4$ in symmetric first mode.

of $m^* \in [3.6, 4.8]$. Based on the correspondence between the decomposed vibrational mode and the mode frequency, the frequency contents around $St = 1$ are related to the chord-wise second mode. The first mode performs at its harmonics with a lower frequency component. We further plot all energetic mode frequencies as a function of m^* in figure 19 (b). In the regime of the second mode, the frequency of the higher-order mode is excited at almost twice the frequency of the dominant mode. This high frequency decreases with an increase of m^* . As the membrane vibration enters the transitional mode, the high-order mode almost vanishes and the first mode frequency content becomes visible. Both energetic frequency components of the first and second modes are observed in the transitional mode regime and the first mode regime. They all have a gradual downward trend and eventually maintain stable values. The percentage of the individual mode energy for the dominant first and second modes in the full membrane vibration is shown in figure 19 (c). The second mode possesses the corresponding mode energy about 24% at $m^* \in [1.5, 2.4]$ and the mode energy reduces to 14.75% for $m^* = 3.6$. Meanwhile, the mode energy of the first mode changes from 0 to 1.6% at $m^* = 3.0$. It is worth noting that the mode energy of the first mode exceeds that of the second mode for $m^* = 4.2$ in the transitional mode regime. Therefore, the predominant mode transitions from the second mode to the first mode. As m^* grows larger than 4.8 and continues to increase, the first mode with the maximum corresponding mode energy always dominates in the membrane vibration during FMI.

5.2.2. Trigger factor of mode transition

The mode transition is confirmed from the mode energy spectra in figure 19 in FMI problems when the inertial effect becomes stronger. The membrane vibration characteristics and the vortex shedding pattern are significantly affected by mass ratio. As a result, the dominant vibrational mode and the wake pattern transition from one aeroelastic mode to another aeroelastic mode triggered by a certain factor. Furthermore, the aerodynamic forces and the full-body profile responses of the flexible membrane

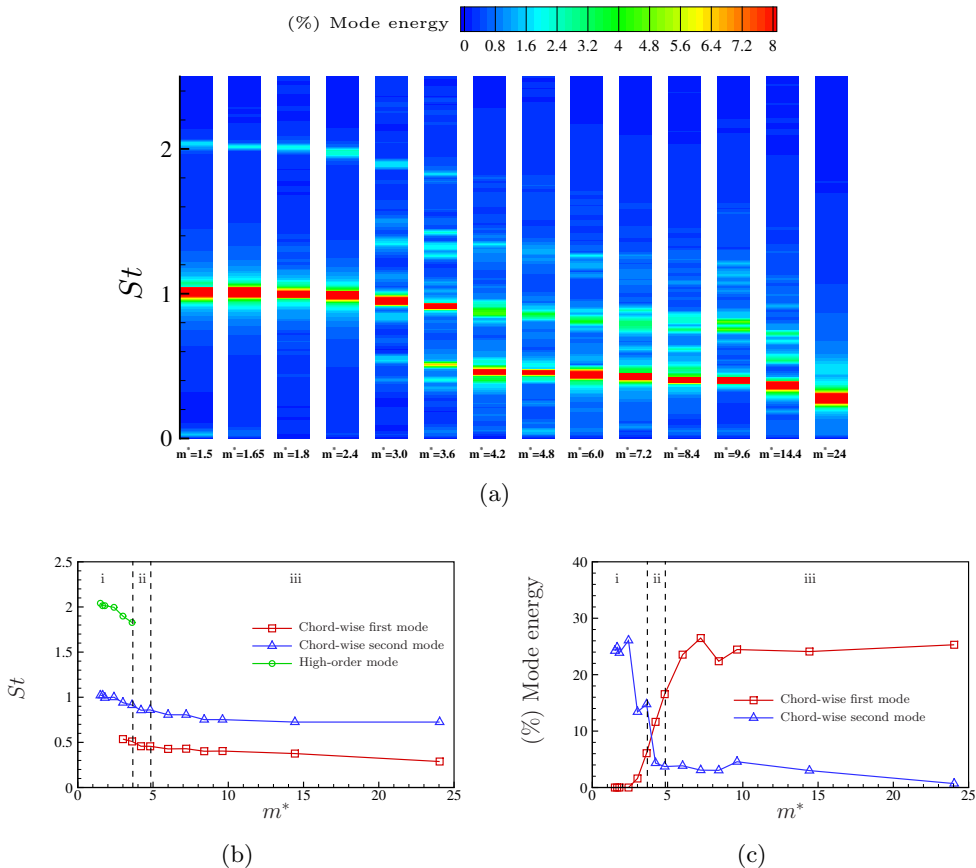


Figure 19: Mode transition map of fluid-membrane coupling system at $\alpha = 15^\circ$ and $Re = 24300$: (a) mode energy spectra, (b) mode frequencies of the obvious membrane modes, (c) mode energies of the dominant first and second modes.

perform different characteristics in different stability regimes as a function of mass ratio m^* . Therefore, it is important to explore how the mode transition is triggered as the relevant aeroelastic parameters change to achieve the desired aeroelastic responses for the flexible membrane. From the results shown in §5.1, we observe the transition between two stability regimes and the vibrational mode transition in the DBS regime. In the following analysis, the reason of the loss of the static stability and the trigger factor of the vibrational mode transition are investigated in detail.

To simplify the complex problem without loss of generality, we consider a 1D membrane with fixed leading and trailing edges extracting from the 3D membrane wing along the chord-wise direction at the mid-span location. The governing equation of the 1D membrane dynamics is written as (Gordnier 2009; Tzezana & Breuer 2019)

$$\rho^s h \frac{\partial^2 \delta_n}{\partial t^2} = T^s \cdot H^s + \Delta p \quad (5.1)$$

where T^s denotes the tension force along the membrane and Δp is the pressure difference between the upper and lower surfaces of the membrane. H^s is the curvature of the

deformed membrane, which is expressed as

$$H^s = \frac{\partial^2 \delta_n}{\partial x^2} \left[1 + \left(\frac{\partial \delta_n}{\partial x} \right)^2 \right]^{-\frac{3}{2}} \quad (5.2)$$

The time-related term on the left side in (5.1) can be negligible since mass ratio has a small value. Thus, the membrane reaches a static-steady state. The steady membrane equation is governed by the Young-Laplace equation, which is reduced from (5.1)

$$T^s \cdot H^s + \Delta p = 0 \quad (5.3)$$

We assume a linear-elastic description for the flexible membrane and substitute $T^s = E^s h (\lambda^s - 1)$ into (5.3) to derive a new governing equation presented as (Waldman & Breuer 2017)

$$Ae + \frac{C_{pd}(\delta_n, \alpha, Re, m^*)}{(\lambda^s(\delta_n) - 1) \cdot H^*(\delta_n)} = 0 \quad (5.4)$$

where $\lambda^s(\delta_n)$ represents the membrane stretch ratio of the length of the deformed segment to the length of the initial undeformed membrane. $H^*(\delta_n)$ is the chord-normalized curvature of the wing and C_{pd} denotes the pressure difference coefficient. The aeroelastic number Ae remains constant for a given FMI problem. This equation describes the relationship between the aerodynamic load acting on the membrane surface and the membrane compliance. Once the aerodynamic load acts on the flexible membrane surface, the flexible membrane statically deforms up to increase the value of $\lambda^s(\delta_n)$ and H^* to resist the aerodynamic load. (5.4) is satisfied and the membrane achieves the DSS when the aerodynamic load is in balance with the intrinsic deformation-induced tension force.

As mass ratio increases to a relatively large value, the effect of the inertial force should be taken into account in FMI problems. The flexible membrane tends to vibrate due to the loss of the static stability. The transition from the DSS regime to the DBS regime can possibly be attributed to the local shear layer instability and the global bluff-body vortex shedding instability (Bohner & Breuer 2019). From the comparison of the instantaneous flow features and the turbulent intensity around the membrane at various mass ratios shown in figure 17 and figure 18, we find that the membrane vibration excites the local shear layer instability at the LE to form a series of large-scale vortices. Meanwhile, the flow fluctuations indicated by the turbulent intensity near the membrane surface become stronger, which sustains the membrane vibration in turn. In addition, the vortex formed at the LE is convected downstream and merges with the TEV to periodically shed into the wake, which is similar to the vortex shedding process behind a bluff body (such as a circular cylinder). This vortex shedding phenomenon is capable of inducing vibration sustainably (Miyawala & Jaiman 2019). As a result, the flexible membrane enters the DBS after leaving the static equilibrium position when mass ratio exceeds the threshold value.

In the DBS regime, the predominant mode of the membrane dynamics transitions to a lower mode as the mass ratio further increases. The term on the left side of (5.1) represents the force induced by the inertial effect, which is related to the mass ratio of the flexible membrane. The two terms on the right side of (5.1) denote the deformation-induced tension force component and the aerodynamic load, respectively. To further investigate how the mass ratio affects the membrane vibrational modes, we plot the tension force coefficient C_T and the aerodynamic force coefficient normal to the wing chord C_N at the mid-span location along the chord-wise direction as a function of mass ratio m^* in figure 20. In figure 20 (a), it is observed that C_T has an almost constant

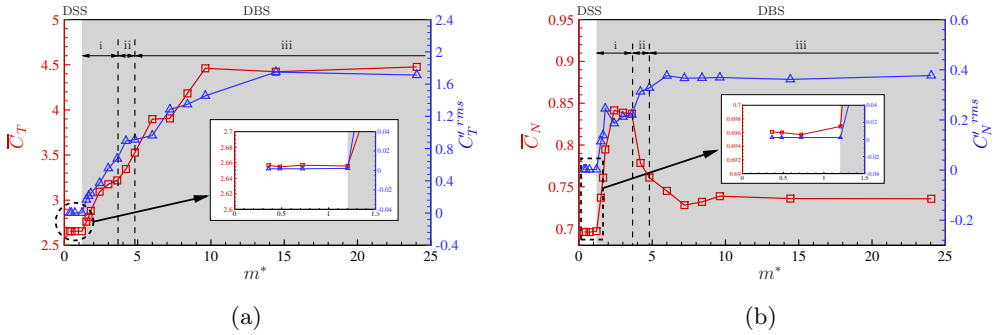


Figure 20: Effect of the mass ratio m^* on: (a) mean tension force coefficient and r.m.s. tension force coefficient fluctuation and (b) mean normal force coefficient and r.m.s. normal force coefficient fluctuation at the mid-span location along the chord-wise direction.

value about 2.65 and the force oscillation indicated by the r.m.s force fluctuation is approximately 0 in DSS. Similar results can be obtained for C_N in this regime. It is worth noting that the oscillations for both forces are no longer 0 in DBS. As the membrane performs the second mode, the mean tension force coefficient increases sharply to 3.22 at $m^*=3.6$ and the mean normal force coefficient firstly rises to 0.84 at $m^* = 2.4$ and then reaches a plain. The mean tension force keeps increasing while the mean normal force coefficient starts to quickly decrease from 0.837 to 0.761 as the membrane vibration enters the transition region. When the predominant mode transitions to the first mode, the mean tension force coefficient grows up and remains almost constant at relatively large mass ratio values. Meanwhile, the mean normal force coefficient reduces to 0.728 at $m^* = 7.2$ and then slightly increases to an approximately constant value.

To gain further insight into the relationship of C_T and C_N , we compare the time history and the mode energy spectrum of both force coefficients corresponding to three different types of vibrational modes in the DBS regime at four specific mass ratio values of $m^*=2.4, 3.6, 4.8$ and 9.6 in figure 21. For $m^*=2.4$ in figure 21 (a), C_T is synchronized with C_N to fluctuate at the same dominant frequency of $St = 0.99$. Meanwhile, C_T shows a clear secondary oscillation component at $St = 1.96$, which has a slightly smaller mode energy than that of the dominant oscillation component observed from figure 21 (b). As the membrane enters the transitional region for $m^* = 3.6$, the time histories of both the force coefficients gradually become disordered with variable amplitudes and frequencies shown in figure 21 (c). The dominant frequency of C_N is still excited at the second modal frequency of $St = 0.91$, but the dominant frequency of C_T with the most mode energy shifts to the higher content of $St = 1.82$. The first modal shape gradually becomes dominant in the membrane vibration as it leaves the transition region at $m^* = 4.8$ and the corresponding frequency is reduced to half the frequency of the second mode. C_N presents the same frequency as the dominant first mode at $St = 0.456$ shown in figure 21 (f). However, two obvious peaks in the mode energy spectrum of C_T are observed and they have similar mode energies. Time history of both force coefficients becomes slightly regular when the flexible membrane achieves a dynamical stable first mode for $m^* = 9.6$ presented in figure 21 (g). The secondary oscillation component is almost vanished in the time history of C_T . In figure 21 (h), the frequency of C_T is twice the frequency of C_N and the first mode.

We compare the dominant Fourier modes for the flexible membrane before and after

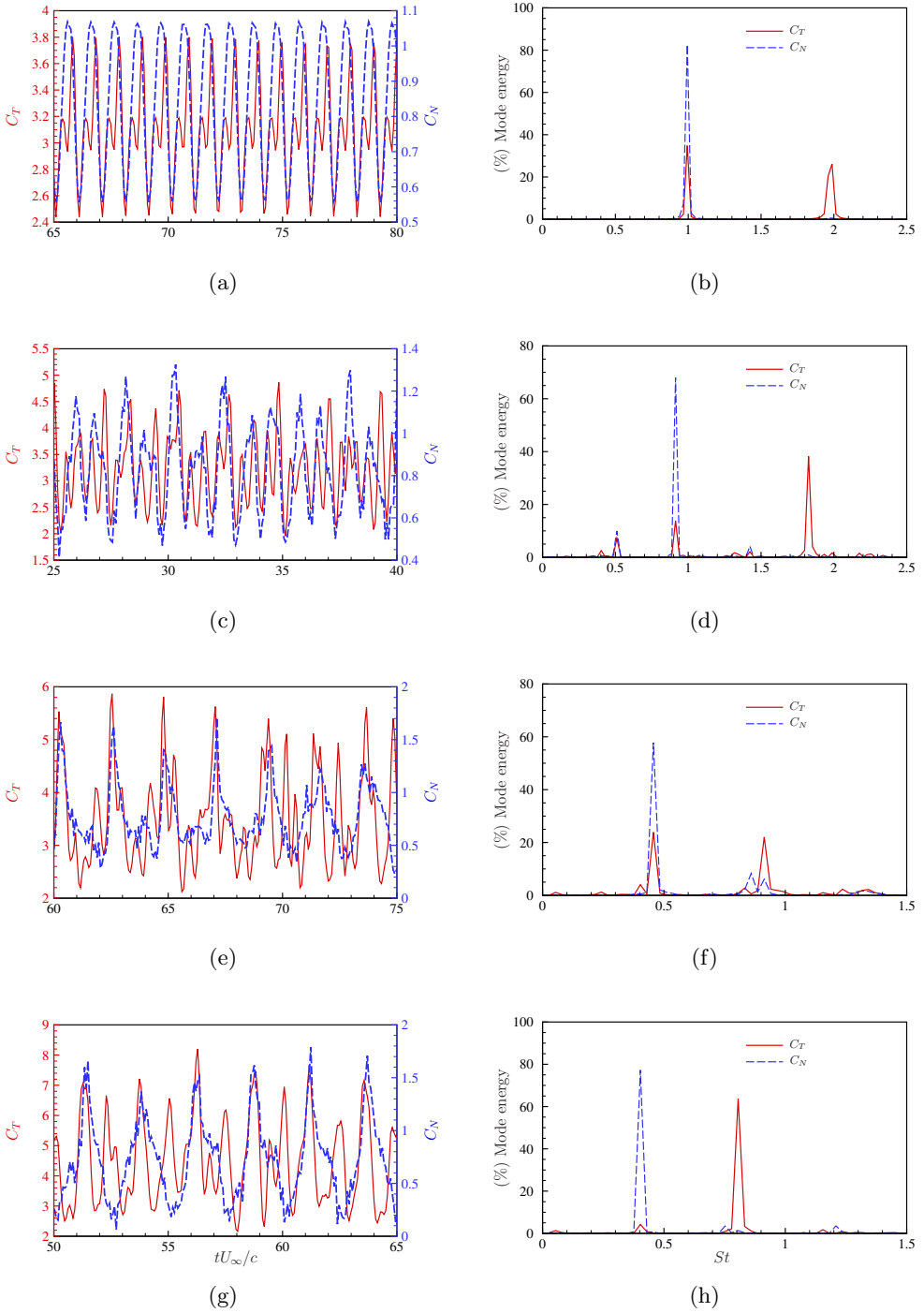


Figure 21: Time history (a,c,e,g) and mode energy spectrum (b,d,f,h) of the tension force coefficient (—) and the normal force coefficient (---) for $m^* =$ (a,b) 2.4, (c,d) 3.6, (e,f) 4.8 and (g,h) 9.6.

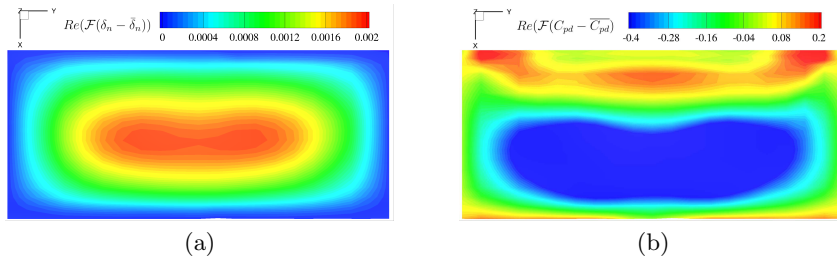


Figure 22: Aeroelastic mode decomposition of 3D flexible membrane for $m^* = 9.6$: (a) the dominant membrane displacement mode and (b) the dominant surface pressure difference mode at $St = 0.4$.

the mode transition. The decomposed aeroelastic modes of the flexible membrane for $m^* = 2.4$ are plotted in figure 8. We extract the dominant aeroelastic modes of the flexible membrane for $m^* = 9.6$ after the mode transition at the frequency peak of $St = 0.4$. The dominant membrane displacement mode and the surface pressure difference mode are presented in figure 22 for the comparison purpose. We observe a first mode for the membrane vibration at $m^* = 9.6$ in figure 22 (a). The red colour region near the LE in the pressure mode is caused by the local shear layer instability. Except for this region, the pressure mode shows a modal shape similar to the displacement mode. This result indicates that the flexible membrane vibration in the first mode is synchronized with the pressure pulsations applied on the membrane surface. From the comparison of the dominant aeroelastic modes for these two typical dynamic mode regimes, we can conclude that the mode transition is triggered by the mode synchronization from the second mode to the first mode as m^* changes.

The energy exchange between the unsteady flow and the membrane vibration is crucial in fluid-membrane coupling problems. We investigate the effect of mass ratio on the power done by the aerodynamic load on the entire membrane in DBS. The instantaneous aerodynamic power coefficient C_{Power} and the period-averaged aerodynamic power coefficient $\overline{C}_{\text{Power}}$ are defined as

$$C_{\text{Power}} = \frac{\int_{\Gamma} (\overline{\boldsymbol{\sigma}}^f \cdot \mathbf{n}) \cdot \mathbf{u}^f d\Gamma}{\frac{1}{2} \rho^f U_{\infty}^3 cb}, \quad \overline{C}_{\text{Power}} = \frac{\frac{1}{T} \int_t^{t+T} (\int_{\Gamma} (\overline{\boldsymbol{\sigma}}^f \cdot \mathbf{n}) \cdot \mathbf{u}^f d\Gamma) dt}{\frac{1}{2} \rho^f U_{\infty}^3 cb} \quad (5.5)$$

where C_{Power} represents the instantaneous aerodynamic power at a transient time instant and $\overline{C}_{\text{Power}}$ reflects the aerodynamic power generated in a completed period.

We evaluate the instantaneous aerodynamic power coefficient C_{Power} and the period-averaged aerodynamic power coefficient $\overline{C}_{\text{Power}}$ for the entire membrane as a function of mass ratio m^* based on (5.5), and the results are shown in figure 23. The period-averaged aerodynamic power coefficient $\overline{C}_{\text{Power}}$ is smaller than 0 in DBS, which eventually shows energy transfer from the membrane vibration to the unsteady air within one completed period. $\overline{C}_{\text{Power}}$ decreases continuously to its minimum value at the end of the transition regime and it grows up by reaching a plain finally. The oscillation amplitude of C_{Power} keeps rising and achieves a constant value at a relatively large m^* . We compare the instantaneous aerodynamic power coefficient C_{Power} within one cycle for five mass ratio values corresponding to three different modes in figure 23 (b). It is worth noting that C_{Power} exhibits positive values in half the cycle and negative values in the other half for all cases. The positive part is related to the overall upward motion and the motion in the negative part shows the opposite direction of the aerodynamic force.

To summarize, the frequency of C_T is synchronized with the frequency of C_N in

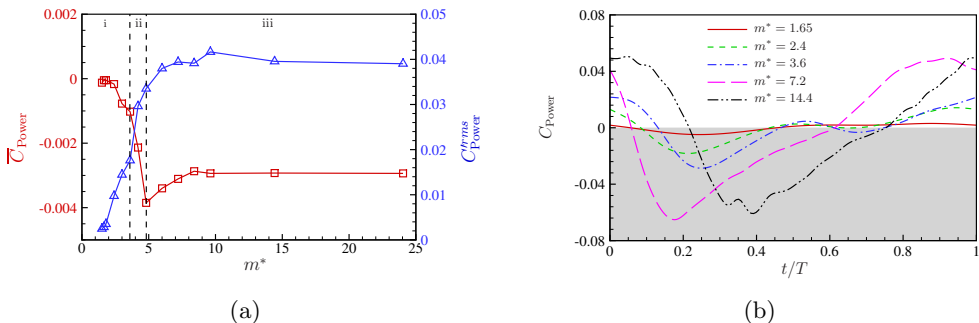


Figure 23: Effect of the mass ratio m^* on: (a) period-averaged aerodynamic power coefficient and r.m.s. instantaneous aerodynamic power coefficient fluctuation, (b) comparison of instantaneous aerodynamic power coefficient within one cycle.

the asymmetric second mode. As the membrane vibration starts to transition to the symmetric first mode, C_T becomes disordered with variable amplitude and frequencies. After the mode transition, the frequency of C_T locks at twice the frequency of C_N in the first mode. Similar mode synchronization phenomenon can be found in the evolution of the flow features around the membrane shown in figure 17 and figure 18 and the mode transition map in figure 19, respectively. As m^* increases, the original mode synchronization process in the second mode is broken by the strong inertial effect, and a new mode synchronization process in the first mode is formed in the membrane vibration through the mode transition.

5.3. Effect of Reynolds number

The nonlinear dynamic behaviours of the flexible membrane exhibit different characteristics at various Reynolds numbers. In this section, we further investigate the effect of Re on the aeroelastic instability and characterize the evolution of the dominant mode and its mode energy. Considering the difference of the dominant mode types for lighter and heavier wings, we conduct a series of studies of Reynolds number effect for the 3D flexible membrane wing at three mass ratios of $m^* = 1.2, 2.4$ and 9.6 within $Re \in [2430, 48600]$. The angle of attack is set to $\alpha = 15^\circ$ and the aeroelastic number is $Ae = 423.14$ for all simulations. The full-body profile responses are plotted to distinguish the membrane vibration state. The mode energy spectra are used to determine the dominant mode and the corresponding mode energy quantitatively with the aid of FMD method.

Figure 24 summarizes the stability regimes of 3D flexible membranes with different mass ratios for a range of Reynolds numbers. In this figure, the curve (---) represents the transition from DSS to DBS. It can be observed that the flexible membrane is prone to lose its static stability at lower Reynolds numbers as the membrane becomes heavier. This is mainly caused by a significantly stronger inertial effect for a heavier membrane. For $m^* = 1.2$, the flexible membrane exhibits high-order modes with relatively small oscillation amplitudes in the DBS regime. It can be inferred that the fluid-membrane coupling effect is weakened when the membrane becomes lighter. For $m^* = 2.4$, the dominant second mode is always observed for the flexible membrane in the DBS regime within the studied Re space. The dominant mode transitions from the second mode to the first mode for $m^* = 9.6$ as Re increases.

To study the mode transition for a heavier membrane with $m^* = 9.6$, we plot the full-body responses and the mode transition map in figure 25 and figure 26, respectively.

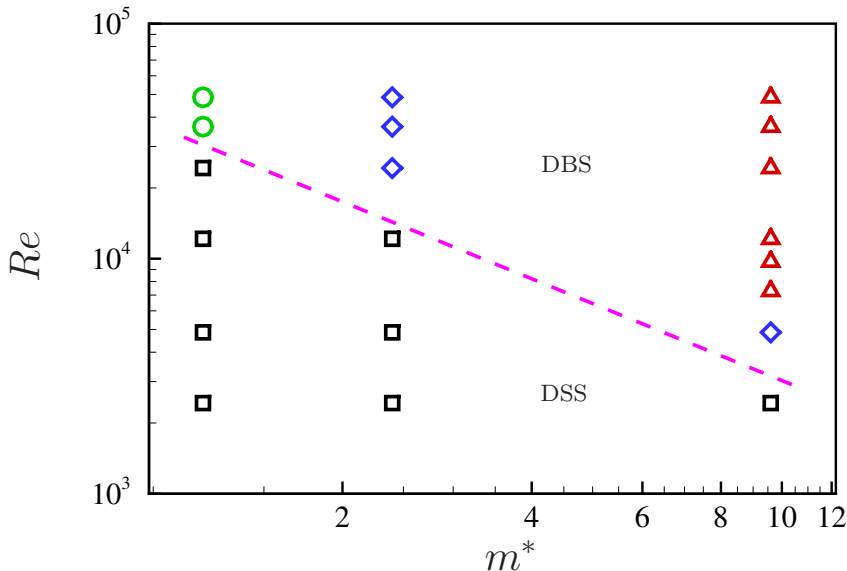


Figure 24: Stability phase diagram: non-dimensional Reynolds number Re versus mass ratio m^* for the 3D flexible membrane at $Ae = 423.14$ for $\alpha = 15^\circ$. Here, the dash line (---) represents the critical Reynolds number for aeroelastic instability. \square denotes the simulation results corresponding to the deformed-steady state. \triangle , \diamond and \circ represent the first, second and high-order modes in the dynamic balance state.

The heavy membrane with $m^* = 9.6$ achieves static stable state at $Re = 2430$, and then it tends to vibrate due to the dynamic instability as shown in figure 25 (a). We observe from the full-body responses that the membrane vibrates in the second mode with a relatively small amplitude for $Re = 4860$. Subsequently, the membrane transitions to the first mode with increasing amplitudes as Re grows up. The mode energy spectra (figure 26 (a)) indicate that the frequency of the dominant mode drops sharply from 1.07 to almost half the value as Re increases from 4860 to 7290. Then, the dominant frequency slightly reduces as Re further increases. Meanwhile, the mode energy of the second mode is much larger than that of the first mode at $Re = 4860$. The mode energy of the first mode rises continuously and exceeds that of the second mode when $Re \geq 7290$. As a result, the mode transition phenomenon is confirmed for the heavy membrane as Re increases.

5.4. Effect of aeroelastic number

Another important parameter that plays a role in the aeroelastic instability is the aeroelastic number Ae , which reflects the rigidity of the flexible membrane. Similar to the diversity of m^* , the membrane component of the flying animals and MAVs possesses a wide range of aeroelastic numbers. In this section, we explore the effect of Ae on the membrane dynamics and the mode transition phenomenon for a light membrane with $m^* = 2.4$ at a moderate angle of attack of 15° and $Re = 24300$ for $Ae \in [84.63, 2115.7]$. The full-body responses and the mode energy spectra as a function of Ae are presented in figure 27 and figure 28, respectively.

The membrane performs the second mode with a continuously decreasing amplitude

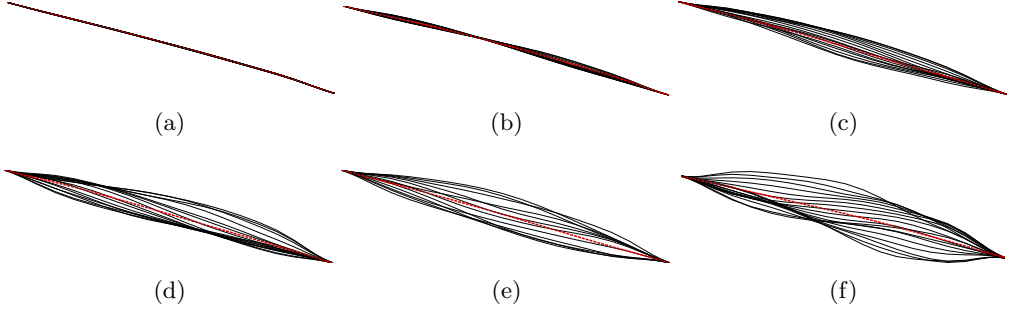


Figure 25: Full-body responses of 3D flexible membrane wing at mid-span location at $\alpha = 15^\circ$, $Ae = 423.14$ and $m^* = 9.6$ for $Re =$ (a) 2430, (b) 4860, (c) 7290, (d) 9720, (e) 12150 and (f) 24300. (---) denotes the time-averaged membrane shape.

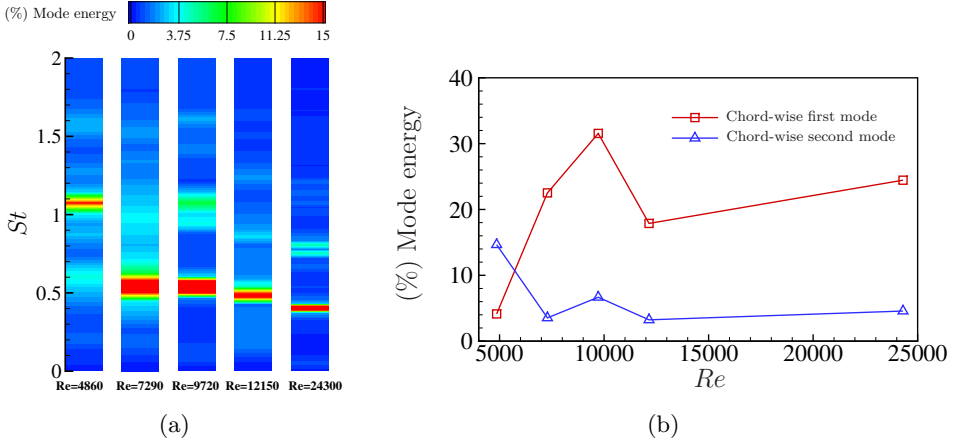


Figure 26: Mode transition map of fluid-membrane coupling system at $\alpha = 15^\circ$, $Ae = 423.14$ and $m^* = 9.6$: (a) mode energy spectra and (b) mode energies of the dominant first and second modes.

for $Ae \in [84.63, 1269.42]$ observed in figure 27. As the aeroelastic number becomes larger to $Ae = 2115.7$, the membrane vibration is suppressed. It achieves a deformed-steady state eventually. Meanwhile, the frequency corresponding to the second mode keeps growing and the mode energy becomes more concentrated at the dominant mode. The second mode shows relatively larger mode energies than the high-order mode for all Ae parameters. Consequently, the second mode dominates the membrane vibration and no mode transition occurs in the parameter space studied. We investigate the evolution of the aeroelastic instability over a wide range of aeroelastic simulation parameters and the mode transition phenomenon is observed in some cases. The mode transition phenomenon is triggered by the mode synchronization interruption for the original dominant aeroelastic mode and the mode synchronization formation for the new dominant aeroelastic mode in FMI. In the next section, we study the mechanism of the fluid-membrane interaction to establish the relationship between the flexible membrane vibration, the pressure fluctuations and the shedding vortex.

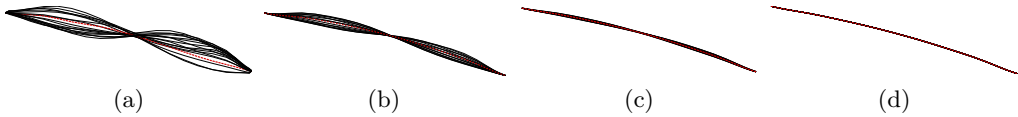


Figure 27: Full-body responses of a 3D flexible membrane wing at mid-span location at $\alpha = 15^\circ$, $m^* = 2.4$ and $Re = 24300$ for $Ae =$ (a) 84.63, (b) 423.14, (c) 1269.42 and (d) 2115.7. (---) denotes the time-averaged membrane shape.

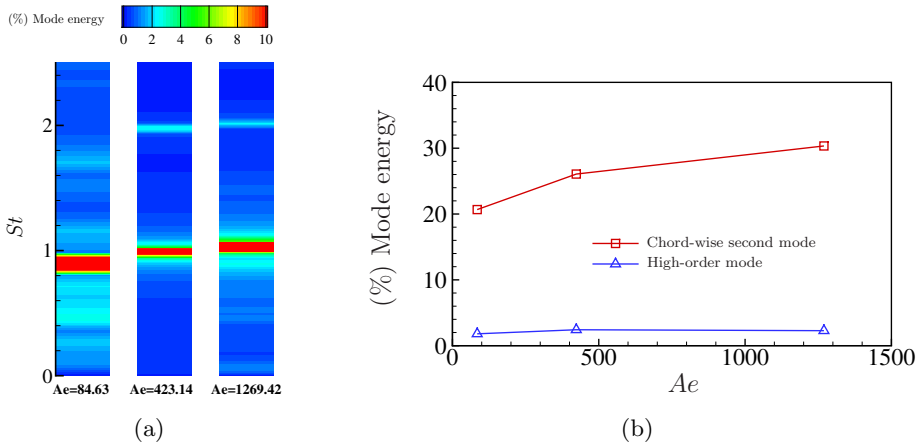


Figure 28: Mode transition map of fluid-membrane coupling system at $\alpha = 15^\circ$, $m^* = 2.4$ and $Re = 24300$: (a) mode energy spectra and (b) mode energies of the dominant chord-wise second mode and high-order mode.

6. Mechanism of fluid-membrane interaction

From §4 and §5, we observe that the flexible membrane experiences a strong coupling with the unsteady flow and the mode synchronization due to the local shear layer instability and the global bluff-body vortex shedding instability. With the aid of the FMD analysis, we find that the membrane vibrational mode and its corresponding surface pressure mode at the same selected frequency of the coupled system exhibit similar modal shapes and wavelengths. Consequently, the aeroelastic modes are excited by the induced pressure pulsations during the interaction between the vortex shedding process and the membrane vibration. The membrane mode transition is triggered during FMI through the mode synchronization as the relevant aeroelastic parameter changes. After we fully understand how the energetic aeroelastic modes are selected in the coupled system and the role of m^* , Re and Ae in the aeroelastic instability, we can deduce a feedback loop between the vibrational mode, the vortex shedding process and the surface pressure fluctuations. In this section, we focus on a highly coupled case at $\alpha = 15^\circ$, $Re = 24300$, $m^* = 2.4$ and $Ae = 423.14$ for brevity to further analyse the correlation between the three parts in the feedback loop. The objective is to investigate the mechanism of FMI.

We perform the global mode decomposition for the membrane vibration, the pressure field and the Y -vorticity field in §4. The result in figure 8 (a) indicates that the predominant fluid and structural Fourier modes of the highly coupled system are excited at the same frequencies. To further study the rolled up vortices at the LE convecting downstream and the TEVs shedding into the wake, we analyse the frequency spectrum

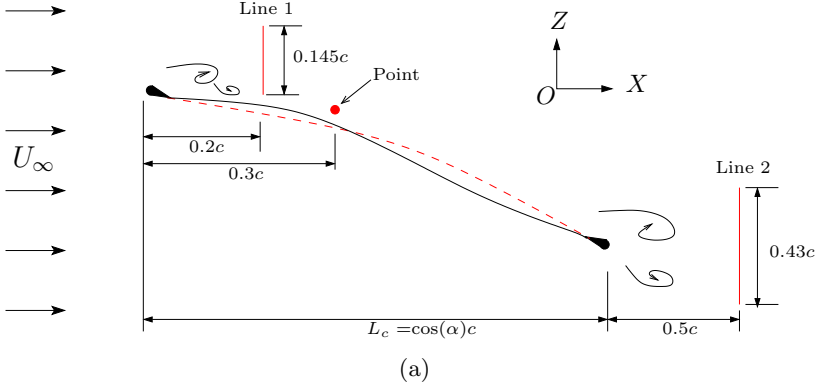


Figure 29: Schematic of the positions of the monitoring lines and point. The red dash line (---) indicates the time-averaged membrane shape. The black solid line (—) represents the instantaneous membrane shape.

of the Y -vorticity along two monitoring lines behind the LE and TE respectively. Figure 29 illustrates the positions of these two monitoring lines in the coupled system on the mid-span plane. Line 1 with a length of $L_1 = 0.145c$ is placed $0.2c$ behind the LE and Line 2 with a length of $L_2 = 0.43c$ is located half chord length behind the TE. Both lines are perpendicular to the direction of the free-stream and they are able to collect the flow fluctuations caused by passing-by vortex structures. 100 monitoring points are evenly distributed along these two lines. 1024 time signal samples are collected at both lines for 37 non-dimensional time units. The spectrogram of Y -vorticity along these two monitoring lines are presented in figure 30. Two non-dimensional vortex shedding frequencies of $St^v = 0.99$ and 1.96 with most concentrated energies are clearly observed almost along the entire lines in the spectrogram. These two frequencies are consistent with the excitation frequencies of the coupled system shown in figure 8 (a). From the comparison in figure 11, the frequency spectrum of the vortex shedding process behind a rigid flat wing shows marked difference with that behind the flexible membrane. The vortex shedding pattern is affected by the membrane flexibility in the coupled system. This result suggests that the membrane vibration is highly coupled with the natural frequency of the vortex shedding phenomenon and its harmonics.

It can be observed from the instantaneous streamlines around the membrane in figure 17 that the pressure fluctuations along the membrane are highly related to the passing-by vortical shedding structures. The global mode decomposition of the pressure field and the Y -vorticity field shown in figure 9 and figure 10 further reveals the relationship of the spatial structures for both fields at the excitation frequencies of the coupled system. Cross-correlation analysis is able to provide further understanding of the relationship between the three parts in the feedback loop. The cross-correlation function of the discrete time signals $x(t_n)$ and $y(t_n)$ is given as

$$R_{xy}(m) = \sum_{n=0}^{N-m-1} x(t_n)y(t_{n+m}) \quad 0 \leq m \leq N-1 \quad (6.1)$$

where $R_{xy}(m)$ is the cross-correlation coefficient and N is the data samples. This

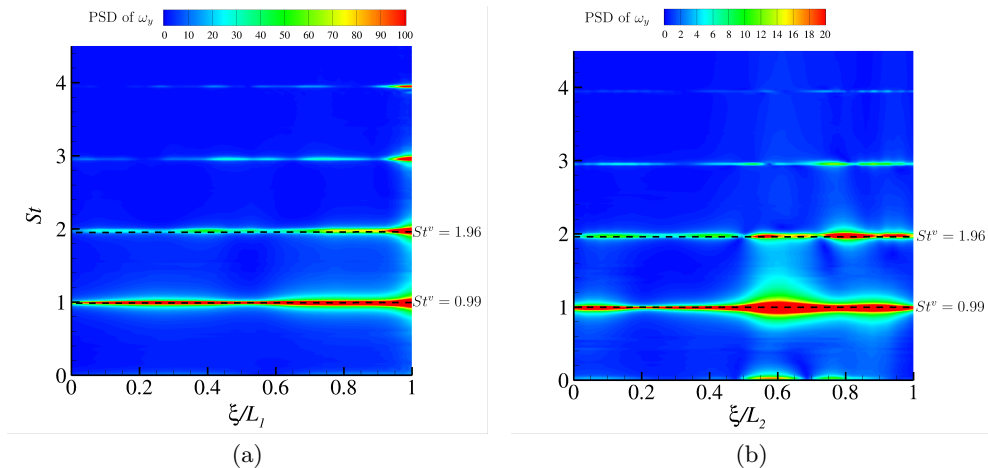


Figure 30: Spectrogram of Y -vorticity along the monitoring lines for $\alpha = 15^\circ$, $Re = 24300$, $m^* = 2.4$ and $Ae = 423.14$ at (a) the leading edge along monitoring Line 1, (b) the trailing edge along monitoring Line 2.

coefficient can be normalized as follows

$$R_{xy}^*(m) = \frac{R_{xy}(m)}{\sqrt{R_{xx}(0)R_{yy}(0)}} \quad (6.2)$$

To examine the correlation between the LEV, the membrane vibration and the pressure pulsation, we calculate the cross-correlations between the Y -vorticity fluctuation time signals at the monitoring point and the membrane deflection fluctuation as well as the pressure fluctuation time signals at 24 points along the membrane upper surface, respectively. The monitoring point is placed $0.3c$ behind the LE at the location with the maximum oscillation amplitude. The normalised cross-correlation coefficients are presented in a 2D contour plot in figure 31, and the x -axis represents the non-dimensional location x/L_c in the direction of the free-stream and y -axis denotes the non-dimensional time shift τ . Strong correlation between the LEV and the deflection along the membrane is observed in figure 31 (a). Since the membrane in the front and rear wings are deflected in opposite directions in the second mode, the sign of the correlation value becomes the opposite sign in the middle of the membrane. We also investigate the correlation between the Y -vorticity at the fixed monitoring point and the pressure time signals along the upper surface in figure 31 (b). The strongest correlation is found at the location near the monitoring point and a negative value is observed at $\tau = 0$ at this location. This result indicates that the clock-wise passing-by vortex leads to negative pressure fluctuations at the same location at the same time.

To complete the feedback loop, we further study the cross-correlation between the membrane deflection time signals at the location of $x/L_c = 0.3$ with maximum standard deviation and the pressure difference fluctuation time signals along the membrane shown in figure 32 (a). The membrane deflection at $x/L_c = 0.3$ has the strongest correlation with the pressure pulsation at the same location. To further understand the relationship between the pressure excitation and the induced membrane vibration, the mode energy spectrum and the cross-correlation of these two variables at $x/L_c = 0.3$ are analysed in figure 32 (b). The spectrum of pressure difference fluctuations is highly consistent with the spectrum of membrane deflection fluctuations. The correlation between these two

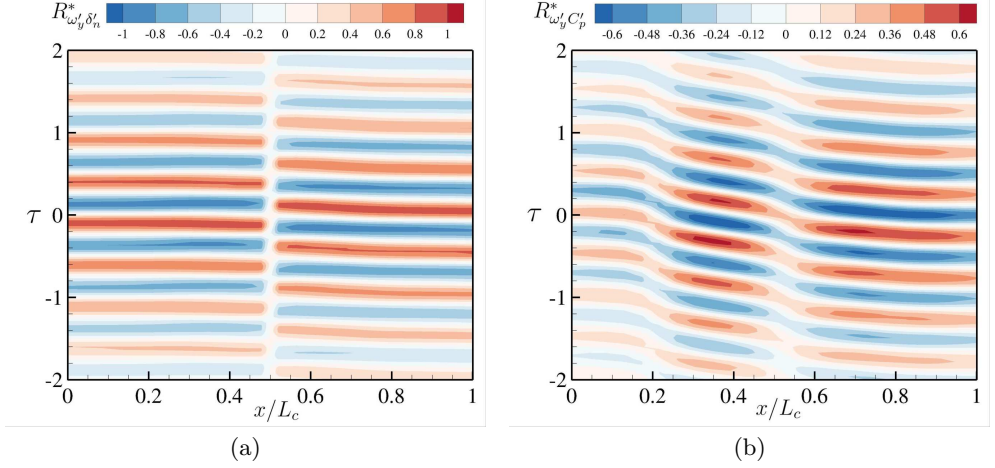


Figure 31: Contours of cross-correlation between (a) the collected time signal data of Y -vorticity fluctuations at monitoring point and the time signal of deflection fluctuations and (b) the collected time signal data of Y -vorticity fluctuations at monitoring point and the time signal of pressure coefficient fluctuations along the membrane upper surface.

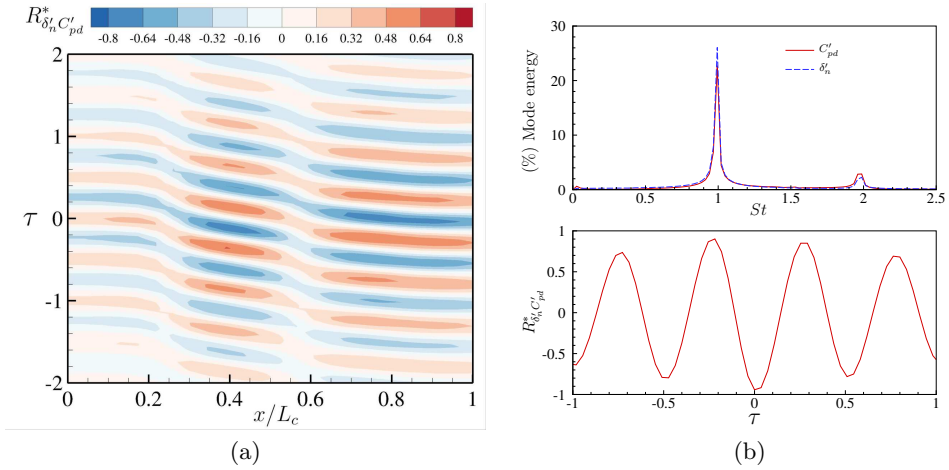


Figure 32: (a) Contours of cross-correlation between the collected time signal data of deflection fluctuations at location $x/L_c = 0.3$ and the time signal of pressure coefficient difference fluctuations along the membrane surface, (b) mode energy spectrum and cross-correlation of the deflection fluctuations and the pressure coefficient difference fluctuations both at location $x/L_c = 0.3$.

variables at the same location is found to be -0.94 with a phase-lag of almost 0° . The result indicates that the instantaneous negative pressure difference fluctuations force the membrane to deform up with positive deflection fluctuations and vice versa. It can be inferred from the above analysis that the pressure difference on membrane surface drives a synchronized membrane vibration in the coupled system.

The investigations of the decomposed aeroelastic mode, the mode selection mechanism, the mode transition phenomenon and the cross-correlation for different variables suggest a feedback loop shown in figure 33 to reveal the coupling mechanisms for FMI problems.

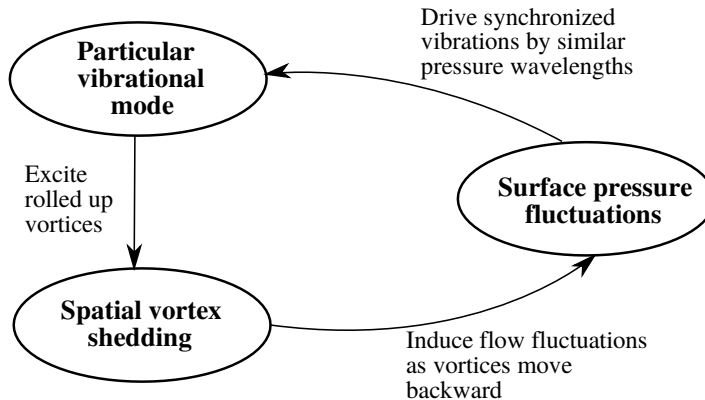


Figure 33: Illustration of a feedback loop of fluid-membrane coupling mechanism.

In this highly coupled system, the membrane vibration in particular vibrational modes excites the separated shear layer to sooner roll up by losing its stability, and then form large-scale vortices. As these vortices detach from the membrane surface and are convected downstream, strong surface pressure fluctuations are induced by the passing-by vortical structures. Subsequently, the flexible membrane is synchronously driven by the pressure pulsations and particular vibration mode is selected by the corresponding pressure mode at the same excitation frequency with a similar wavelength in the coupled system. Furthermore, the dominant leading vortex shedding frequency is found to lock-in with the membrane vibration frequency of the selected membrane mode. As a result, a dynamic balance between the external aerodynamic load and the flow-induced tension is achieved to sustain the large-amplitude membrane vibration.

7. Conclusions

We have investigated the flow-induced vibrations and the aeroelastic instability of a 3D flexible membrane wing in an unsteady viscous incompressible flow through a series of numerical simulations. The four edges of the 3D rectangular flexible membrane were glued to a rigid supporting frame with no pretension at a moderate angle of attack of $\alpha = 15^\circ$. We found that the flexible membrane exhibited complex vibrational responses due to the overlapping modes excited by the unsteady flow with various flow scales. A global mode decomposition method based on the Fourier transform was employed to decompose the full membrane dynamics into frequency-ranked aeroelastic modes in the spatio-frequency domain. The contribution of each aeroelastic mode to the overall membrane responses was evaluated and the dominant aeroelastic modes were identified at the excitation frequency with most mode energies from the mode energy spectrum. This mode decomposition algorithm built a direct connection between the fluid and structural Fourier modes via the correspondence at the same excitation frequency. Compared to the mode energy spectrum of a rigid flat wing, the surface pressure fluctuation and the spatial Y -vorticity with continuously distributed frequencies were redistributed into the dominant frequency and its harmonics of the membrane vibration for the coupled system. It was observed from the decomposed aeroelastic modes for both wings that high-intensity pressure fluctuations became closer to the flexible membrane surface and the wake patterns were significantly changed due to the flexibility effect. Furthermore, the aeroelastic mode was selected by the strong coupling effect and the mode synchronization

between the surface pressure excitations and the membrane vibrations with similar modal shapes and wavelengths at the same frequency.

With the aid of the FMD method, we further studied the evolution of the flow-excited membrane aeroelastic instability as a function of mass ratio m^* . Two distinctive stability regimes were identified from the full-body profile responses, namely (a) deformed-steady state (DSS) and (b) dynamic balance state (DBS) for $m^* \in [0.36, 24]$. The aerodynamic forces and the membrane deformations kept constant with no obvious oscillation in the DSS regime at a low mass ratio region of $m^* \in [0.36, 1.2]$. The detached vortex was far away from the membrane surface and the pressure fluctuation on the membrane surface was very weak. We found the aerodynamic load was in balance with the inherent tension force as the flexible membrane statically deformed up to an equilibrium position through a linear elastic analysis. As m^* exceeded the critical value of 1.2, the original static balance between the tension force and the aerodynamic load was broken when the stronger inertial effect was taken into account. Thus, the local separated shear layer was excited by the membrane vibration in the proximate of the LE, causing it to sooner roll up and generated a chain of vortices convecting downstream, leading to global bluff-body vortex shedding instability. In turn, the membrane vibration with DBS was sustained by the high-intensity fluctuating shear layer near the membrane surface. We further identified three distinctive vibrational modes within the DBS regime as a function of increasing m^* : (i) asymmetric chord-wise second mode, (ii) transitional mode and (iii) symmetric chord-wise first mode. The aerodynamic characteristics and the membrane vibrations were significantly affected by the inertial effect. The maximum lift coefficient and the optimal aerodynamic efficiency were achieved as the membrane tended to transition to the symmetric first mode. We further employed the FMD method to evaluate the contribution of each energetic mode to the full membrane responses. The evolution of the mode frequencies and the energies of the dominant modes in the mode transition map indicated that the first mode competed with the second mode and became dominant in the membrane vibration through the transitional region as the membrane got heavier. With the help of a 1D membrane dynamic model, we found the pressure fluctuations acting on the membrane surface and the flow-induced tension dominated the characteristics of the membrane vibration. The tension force gradually became desynchronized with the normal force in the mode transition region and its dominant frequency locked at twice the frequency of the membrane vibration in the symmetric first mode. Moreover, we studied the membrane instability as a function of Re for a membrane with three different mass ratios to obtain the stability phase diagram. The effect of aeroelastic number Ae was also investigated for a light wing with $m^* = 2.4$. A similar mode transition phenomenon was observed for the heavy membrane with $m^* = 9.6$ as a function of Re .

The frequency characteristics of the LEV and the TEV were analysed by computing the spectrogram of Y -vorticity along two monitoring lines. The vortex lock-in phenomenon was observed as the vortex shedding frequency was consistent with the membrane vibration frequency. We further calculated the cross-correlation between the Y -vorticity fluctuation, the membrane deflection fluctuation and the pressure fluctuation time signals. The results indicated that these three physical variables were strongly correlated and had synchronized fluctuations. Based on all the mentioned analysis, we suggested a feedback loop between the membrane vibration mode, the vortex shedding process and the surface pressure fluctuations to reveal the mechanism of the flow-induced vibration for a strongly coupled system. The mode synchronization process could be affected by changing one or several of the three key parts in the feedback loop to trigger the mode transition finally. From both operations and design perspectives, this feedback

loop offered a possible control way to change the membrane dynamic responses and the aerodynamic characteristics by enhancing or suppressing individual spatial aeroelastic modes for flexible membranes in separated flow conditions.

Acknowledgements

The authors wish to acknowledge supports from the National University of Singapore and the Ministry of Education, Singapore.

Declaration of interests

The authors report no conflict of interest.

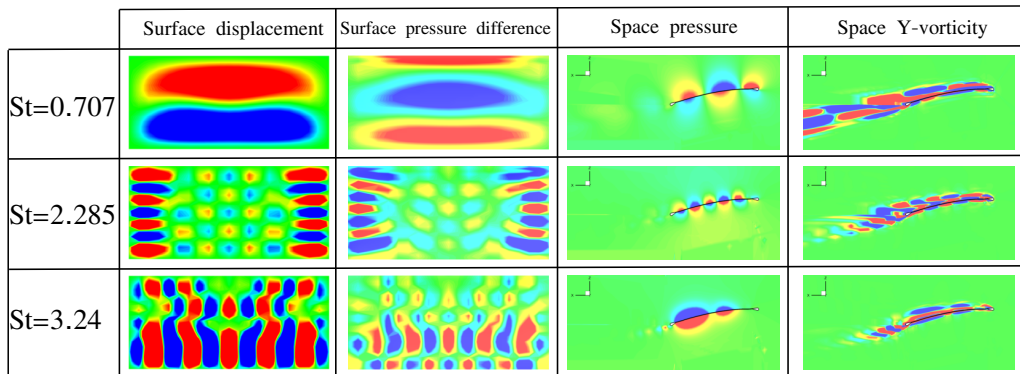
REFERENCES

- ANDERSEN, A. , BOHR, T. , SCHNIPPER, T. & WALTHER, J. H. 2017 Wake structure and thrust generation of a flapping foil in two-dimensional flow. *J. Fluid Mech.* **812**.
- ARBÓS-TORRENT, S. , GANAPATHISUBRAMANI, B. & PALACIOS, R. 2013 Leading-and trailing-edge effects on the aeromechanics of membrane aerofoils. *J. Fluids Struct.* **38**, 107–126.
- BAHLMAN, J. W. , SWARTZ, S. M. & BREUER, K. S. 2013 Design and characterization of a multi-articulated robotic bat wing. *Bioinspir. Biomim* **8** (1), 016009.
- BLEISCHWITZ, R. , DE KAT, R. & GANAPATHISUBRAMANI, B. 2015 Aspect-ratio effects on aeromechanics of membrane wings at moderate reynolds numbers. *AIAA J.* **53** (3), 780–788.
- BOHNKER, J. R. & BREUER, K. S. 2019 Control of separated flow using actuated compliant membrane wings. *AIAA J.* **57** (9), 3801–3811.
- DONG, H. , MITTAL, R. & NAJJAR, F. 2006 Wake topology and hydrodynamic performance of low-aspect-ratio flapping foils. *J. Fluid Mech.* **566**, 309–343.
- GORDNIER, R. E. 2009 High fidelity computational simulation of a membrane wing airfoil. *J. Fluids Struct.* **25** (5), 897–917.
- GORDNIER, R. E. & ATTAR, P. J. 2014 Impact of flexibility on the aerodynamics of an aspect ratio two membrane wing. *J. Fluids Struct.* **45**, 138–152.
- GRAFF, K. F. 2012 *Wave motion in elastic solids*. Courier Corporation.
- GURUGUBELLI, P. & JAIMAN, R. 2015 Self-induced flapping dynamics of a flexible inverted foil in a uniform flow. *J. Fluid Mech.* **781**, 657–694.
- HE, X. , GUO, Q. & WANG, J. 2019 Extended flexible trailing-edge on the flow structures of an airfoil at high angle of attack. *Exp. Fluids.* **60** (8), 122.
- JAIMAN, R. , PILLALAMARRI, N. & GUAN, M. 2016 A stable second-order partitioned iterative scheme for freely vibrating low-mass bluff bodies in a uniform flow. *Comput. Method. Appl. M.* **301**, 187–215.
- KINSLER, L. E. , FREY, A. R. , COPPENS, A. B. & SANDERS, J. V. 1999 Fundamentals of acoustics. *Fundamentals of Acoustics, 4th Edition, by Lawrence E. Kinsler, Austin R. Frey, Alan B. Coppens, James V. Sanders, pp. 560. ISBN 0-471-84789-5. Wiley-VCH, December 1999.* p. 560.
- LI, G. , KHOO, B. C. & JAIMAN, R. K. 2020 Computational aeroelasticity of flexible membrane wings at moderate reynolds numbers. In *AIAA Scitech 2020 Forum*, p. 2036.
- LI, G. , LAW, Y. Z. & JAIMAN, R. K. 2019 A novel 3d variational aeroelastic framework for flexible multibody dynamics: Application to bat-like flapping dynamics. *Comput. Fluids.* **180**, 96–116.
- LIU, B. & JAIMAN, R. 2018 Dynamics and stability of gap-flow interference in a vibrating side-by-side arrangement of two circular cylinders. *J. Fluid Mech.* **855**, 804–838.
- MA, L. , FENG, L. , PAN, C. , GAO, Q. & WANG, J. 2015 Fourier mode decomposition of piv data. *Sci. China Technol. Sci.* **58** (11), 1935–1948.
- MIYANAWALA, T. P. & JAIMAN, R. K. 2019 Decomposition of wake dynamics in fluid–structure interaction via low-dimensional models. *J. Fluid Mech.* **867**, 723–764.

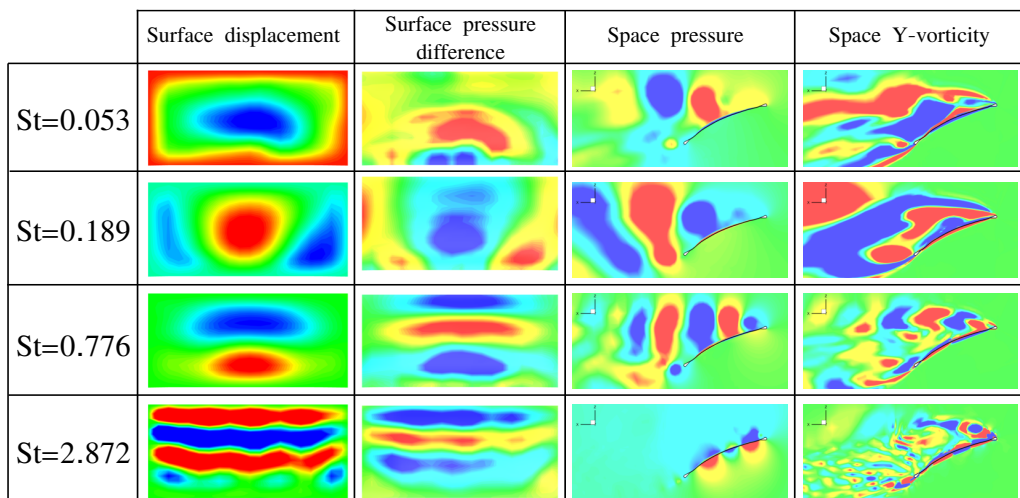
- NEWMAN, B. G. 1987 Aerodynamic theory for membranes and sails. *Prog. Aerosp. Sci.* **24** (1), 1–27.
- ROJRATSIRIKUL, P. , GENÇ, M. , WANG, Z. & GURSUL, I. 2011 Flow-induced vibrations of low aspect ratio rectangular membrane wings. *J. Fluids Struct.* **27** (8), 1296–1309.
- ROJRATSIRIKUL, P. , WANG, Z. & GURSUL, I. 2009 Unsteady fluid–structure interactions of membrane airfoils at low reynolds numbers. *Exp. Fluids.* **46** (5), 859.
- ROJRATSIRIKUL, P. , WANG, Z. & GURSUL, I. 2010a Effect of pre-strain and excess length on unsteady fluid–structure interactions of membrane airfoils. *J. Fluids Struct.* **26** (3), 359–376.
- ROJRATSIRIKUL, P. , WANG, Z. & GURSUL, I. 2010b Unsteady aerodynamics of low aspect ratio membrane wings. In 48th AIAA Aerospace Sciences Meeting Including the New Horizons Forum and Aerospace Exposition, p. 729.
- SERRANO GALIANO, S. & SANDBERG, R. D. 2016 Effect of the leading and trailing edge geometry on the fluid-structural coupling of membrane aerofoils. In 54th AIAA Aerospace Sciences Meeting, p. 0853.
- SERRANO-GALIANO, S. , SANDHAM, N. D. & SANDBERG, R. D. 2018 Fluid–structure coupling mechanism and its aerodynamic effect on membrane aerofoils. *J. Fluid Mech.* **848**, 1127–1156.
- SHYY, W. , BERG, M. & LJUNGVIST, D. 1999 Flapping and flexible wings for biological and micro air vehicles. *Prog. Aerosp. Sci.* **35** (5), 455–505.
- SMITH, R. & SHYY, W. 1995 Computational model of flexible membrane wings in steady laminar flow. *AIAA J.* **33** (10), 1769–1777.
- SONG, A. , TIAN, X. , ISRAELI, E. , GALVAO, R. , BISHOP, K. , SWARTZ, S. & BREUER, K. 2008 Aeromechanics of membrane wings with implications for animal flight. *AIAA J.* **46** (8), 2096–2106.
- SUN, X. , REN, X.-L. & ZHANG, J.-Z. 2017 Nonlinear dynamic responses of a perimeter-reinforced membrane wing in laminar flows. *Nonlinear Dyn.* **88** (1), 749–776.
- SUN, X. & ZHANG, J. 2017 Effect of the reinforced leading or trailing edge on the aerodynamic performance of a perimeter-reinforced membrane wing. *J. Fluids Struct.* **68**, 90–112.
- SUN, X. & ZHANG, J.-z. 2016 Nonlinear vibrations of a flexible membrane under periodic load. *Nonlinear Dyn.* **85** (4), 2467–2486.
- TIOMKIN, S. & RAVEH, D. E. 2019 On membrane-wing stability in laminar flow. *J. Fluids Struct.* **91**.
- TREGIDGO, L. , WANG, Z. & GURSUL, I. 2011 Fluid-structure interactions for a low aspect-ratio membrane wing at low reynolds numbers. In 41st AIAA Fluid Dynamics Conference and Exhibit, p. 3436.
- TREGIDGO, L. , WANG, Z. & GURSUL, I. 2013 Unsteady fluid–structure interactions of a pitching membrane wing. *Aerosp. Sci. Technol.* **28** (1), 79–90.
- TZEZANA, G. A. & BREUER, K. S. 2019 Thrust, drag and wake structure in flapping compliant membrane wings. *J. Fluid Mech.* **862**, 871–888.
- WALDMAN, R. M. & BREUER, K. S. 2017 Camber and aerodynamic performance of compliant membrane wings. *J. Fluids Struct.* **68**, 390–402.
- WEBSTER, F. A. & GRIFFIN, D. R. 1962 The role of the flight membranes in insect capture by bats. *Anim. Behav.* **10** (3-4), 332–340.
- YANG, H. , DUDLEY, J. & HARRIS, R. 2018 Aeroelasticity validation study for a three-dimensional membrane wing. *AIAA J.* **56** (6), 2361–2371.
- ZHANG, Q. , LIU, Y. & WANG, S. 2014 The identification of coherent structures using proper orthogonal decomposition and dynamic mode decomposition. *J. Fluids Struct.* **49**, 53–72.

Appendix A. Decomposed aeroelastic modes

In this appendix, we further provide the decomposed aeroelastic modes for the 3D flexible membrane at $\alpha = 10^\circ$ and $\alpha = 25^\circ$ to support the proposed aeroelastic mode selection mechanism. The decomposed aeroelastic modes corresponding to the surface displacement, surface pressure coefficient difference, the pressure and the Y-vorticity on the mid-span plane for the flexible membrane are presented in figure 34.



(a)



(b)

Figure 34: Aeroelastic mode decomposition and dominant mode identification of fluid-membrane interaction for $Re = 24300$, $m^* = 2.4$ and $Ae = 423.14$ at (a) $\alpha = 10^\circ$ and (b) $\alpha = 25^\circ$.

Several aeroelastic modes with obvious mode energies at corresponding non-dimensional frequencies are selected for a demonstration purpose.

It can be observed from figure 34 that the structural modes exhibit modal shapes similar to the surface pressure modes at different frequencies. The obvious difference between the modal shapes is noticed for the aeroelastic modes at $St = 0.707$ for $\alpha = 10^\circ$. Due to the existence of the local shear layer instability, a small pressure perturbation region is observed at the LE. Despite this difference, the modal shapes for the fluid and structural modes show high correlations. Similar results can be found in the decomposed aeroelastic modes at $\alpha = 25^\circ$ in figure 34 (b). We conclude from the decomposed aeroelastic modes that the mode selection mechanism is crucial in the excitations of the membrane vibration and the pressure fluctuation in the coupled system.